

4-2020

Investigation of Selective Laser Melting Fabricated Internal Cooling Channels

Colin Jack
Grand Valley State University

Follow this and additional works at: <https://scholarworks.gvsu.edu/theses>



Part of the [Materials Science and Engineering Commons](#)

ScholarWorks Citation

Jack, Colin, "Investigation of Selective Laser Melting Fabricated Internal Cooling Channels" (2020).
Masters Theses. 971.
<https://scholarworks.gvsu.edu/theses/971>

This Thesis is brought to you for free and open access by the Graduate Research and Creative Practice at ScholarWorks@GVSU. It has been accepted for inclusion in Masters Theses by an authorized administrator of ScholarWorks@GVSU. For more information, please contact scholarworks@gvsu.edu.

Investigation of Selective Laser Melting Fabricated Internal Cooling Channels

Colin Jack

A Master's Thesis Submitted to the Graduate Faculty of

GRAND VALLEY STATE UNIVERSITY

In

Partial Fulfillment of the Requirements

For the Degree of

Engineering, M.S.E./B.S.E. Articulated

Padnos College of Engineering and Computing

April 2020

Acknowledgements

I would like to express my deep gratitude to Dr. Pung for his guidance and resourcefulness throughout the arduous process of this investigation.

I would also like to thank Dr. Hugh Jack and the Western Carolina University College of Engineering and Technology for assisting in the complex fabrication of the additively manufactured experimental samples.

Lastly, I would like to extend this gratitude to my friends and family who inspire me and drive me to pursue great challenges.

Abstract

Channels where coolant is run to cool a system are common in injection mold tooling. Conventionally, these channels are machined into the mold. This has limited the design of mold cooling systems to the constraints of traditional machining processes, where straight circular channels machined from cast material are typical. The transfer of heat away from the part cavity into these cooling channels has a large effect on the cooling time of the injection mold cycle. In this investigation, laser powder bed fusion processes were used to create non-circular cooling channels. To compare cooling performance, elliptical and circular channels of equal cross-sectional area were investigated for mass flow rate and rate of heat transfer. Between conventionally machined and additively manufactured channels, surface roughness of the channel wall and condition of the parent material were investigated as potential factors as well. Through simulation, analysis of channel surface roughness, and experimentation, the results indicated that: the channel machined from cast 316L stainless steel had higher flow rate and rate of heat transfer compared to the machined channel fabricated from selective laser melting 316L metal powder, the machined channel had higher flow rate and rate of heat transfer compared to the as-fabricated additively manufactured sample, and the circular additively manufactured channel had higher flow rate and rate of heat transfer compared to the elliptical channel. Overall, the traditionally machined circular channels had superior cooling performance than the additively manufactured elliptical channels. However, the results demonstrate that changing the length-to-width ratio of elliptical cross channels can be used to locally control cooling on regions of the part to reduce hot-spots in the mold and part defects.

Table of Contents

CHAPTER 1. INTRODUCTION	13
Statement of the Problem.....	13
Injection molding	13
Alternative Applications	14
Research Objectives.....	15
References.....	16
CHAPTER 2. Literature Review	17
Additive Manufacturing Definitions.....	18
History of Additive Manufacturing for Conformal Cooling.....	20
Flow of Coolant through a Channel.....	22
Darcy–Weisbach Equation.....	22
Hydraulic Diameter.....	23
Pipe Friction Factor.....	23
Moody Chart	24
Proposed Models for Friction Turbulence	25
Model of Cooling for a Cooling Channel	27
Overall Rate of Convection Heat Transfer	27
Convection Cooling and the Nusselt Number	27
Approximations from Previous Research	29
Conduction of a Cooling Cell	31
SLM Factors and Existing Case Studies	32
Material Characteristics of Laser Powder Bed Parts	32
Thermal Conductivity of Machined versus Powdered Metals.....	33
Typical Input parameters for Injection Mold Cooling.....	34

Surface Roughness of Channel Wall	35
Process Recommendations for Laser Powder Bed Fusion Processes	38
Build orientation and material support considerations	38
Experimental Parameters	39
Optimal cross sections for laser powder bed fusion processes	41
Surface roughness as a function of build angle	42
Unsupported features	42
References	44
CHAPTER 3. EXPERIMENTAL INVESTIGATION AND COMPUTER SIMULATION	47
Inputs and Outputs	47
Fixed Inputs	47
Outputs	48
Simulation	48
Methodology	48
Model geometry	48
Meshing of Simulated Model.....	49
Computation of Simulated Model.....	50
Residuals of CFD model.....	52
Limitations of CFD model	53
Validation of CFD Results.....	53
CFD Results	55
Creation of Experimental Parts	61
Fabrication of Machined Cooling Block.....	61
Build Conditions of Additively Manufactured Parts	61
Calculation of Supported Surface Roughness.....	66

Surface Roughness Measurements of Various Build Angles	68
Approximating Average Roughness of Cooling Channel	71
Verification of Roughness Analysis	72
Roughness Testing of Sample Channels.....	72
Morphology of Experimental Cooling Channels	76
Experimental Methodology	77
Experimental Parameters	81
Calibration of Thermocouples	83
References.....	83
CHAPTER 4. RESULTS AND DISCUSSION.....	84
Conclusions.....	89
Future Work.....	90
Appendix A – Design of experimental and simulated parts	93
Appendix B – Surface Roughness Data and Example Calculation	94
Appendix C – Arduino code for thermocouple measurements.....	98
Appendix D: Experimental Data Example and Calibrations	101

List of Tables

Table 1: Key process parameters for laser powder bed fusion of metals.	33
Table 2: Inputs for design of injection mold cooling systems.	34
Table 3: Outputs for design of injection mold cooling systems.	35
Table 4: DMLS Design Recommendations for the EOS M 290.	40
Table 5: Geometry of various elliptical cross-sections of equal area.	41
Table 6: Unsupported internal features of various elliptical channels of equal cross-sectional area.	43
Table 7: Fixed inputs.	47
Table 8: Outputs in comparing elliptical cooling channels.	48

Table 9: Mesh statistics.....	49
Table 10: Model configuration for simulation.....	50
Table 11: Bodies, boundaries, and conditions of CFD model.....	51
Table 12: Material properties for simulation.....	52
Table 13: Solution methods.....	52
Table 14: Mesh quality of various runs and the resulting CFD outputs.....	54
Table 15: Results of simulation.....	56
Table 16: Experimental cooling blocks.....	64
Table 17: Machine conditions for EOS M 290.....	65
Table 18: Laser speed, power, and hatch distance for various geometries.....	66
Table 19: Equations and R^2 values for 2 nd order polynomial models.....	71
Table 20: Comparison of theoretical average R_a and R_z values for the supported wall of various elliptical cross sections.....	72
Table 21: Percent difference between measured surface roughness of C3 and the models for roughness.....	76
Table 22: Photomicrographs of C1-C4 at four different build regions.....	77
Table 23: Experimental Apparatus.....	80
Table 24: Experimental values.....	82
Table 25: Experimental rates of heat transfer.....	84
Table 26: Experimental flow rates.....	84
Table 27: Comparison of results from simulation and experimentation.....	88

List of Figures

Figure 1: Experimental cross-sections of a micro-heat pipe.....	15
Figure 2: Visual comparison of the minimum cavity-to-cooling-channel distance for (a) conventionally cooled molds and (b) additively manufactured conformally cooled molds.	17
Figure 3: Example build angles of various surfaces.	19
Figure 4: Cast aluminum molds, used to assess cooling performance of a semi-circular cooling channel.	21
Figure 5: Moody chart [8].....	25
Figure 6: Experimental data in Nikuradse’s experimental friction-turbulence model.	26
Figure 7: A relationship schematic along a Nikurdase Curve across the spectrum of turbulent energy, roughness, thickness of viscous layer, and dominant eddie size.	26
Figure 8: Nusselt number vs. Reynolds number for air-cooled DMLS surfaces of various roughnesses [3]. The $R_a=1\mu\text{m}$ sample was milled post-build for comparison.	28
Figure 9: A cooling cell for a circular cooling channel.	31
Figure 10: Surface morphology of 316L stainless steel, fabricated with SLM. (a) shows a surface without re-melting. (b) shows the surface of a re-molten part.....	36
Figure 11: Internal feature design guide for EOS M290 [18]. (a) and (b) depict rough surfaces for unsupported faces. (c) shows a hole smaller than 6mm – ideally small enough to not require supports. (d) shows a larger hole where support structures are used to support the feature.....	37
Figure 12: Vertical build orientations provide the best surface finish [18].	38
Figure 13: Unsupported feature, seen in the cross-section of a powdered metal cooling channel.	43
Figure 14: Model residual convergence for (a) 6x6mm circular channel and (b) 20x1.8mm elliptical channel.	53
Figure 15: Percent difference in CFD results vs. mesh elements.	55
Figure 16: Thermal contours of outer boundaries for 6x6mm simulation.....	57
Figure 17: Thermal contours of outer boundaries for 20x1.8mm simulation.....	58
Figure 18: Thermal contours of mid-channel slices for 6x6mm simulation.....	59
Figure 19: Thermal contours of mid-channel slices for 6x6mm simulation.....	59

Figure 20: Velocity magnitude contour of front-view mid-channel slice for 20x1.8mm simulation.	60
Figure 21: Velocity magnitude countour of front-view mid-channel slice for 20x1.8mm simulation.	60
Figure 22: Build orientation of additively manufacturing cooling channels.	62
Figure 23: Build orientation of surface roughness test pieces: E1, E2, E3, and E4.	63
Figure 24: Delamination of failed parts from the raft due to thermal stress.	63
Figure 25: Thermal fin and raft pattern on successfully fabricated parts.	64
Figure 26: CAD model of build-angle to surface roughness test parts. (a) isometric view of E1, E2, E3, and E4 (b) (c) cross sections of E1 showing positive (red) and negative (purple) build surfaces	67
Figure 27: Measurement of surface roughness setup (a) parallel to the direction of incline and (b) perpendicular to the direction of incline.	68
Figure 28: R_a data for various supported angles.	69
Figure 29: R_z data for various supported angles.	70
Figure 30: R_a surface roughness at various angles for C1, C2, and C3.	73
Figure 31: R_z surface roughness at various angles for C1, C2, and C3.	74
Figure 32: R_a surface roughness of C3 compared to the model.	75
Figure 33: R_z surface roughness of C3 compared to the model.	75
Figure 34: Experimental diagram and the placement of various measurements.	78
Figure 35: Experimental setup.	79

Nomenclature

A	Cross sectional area (m ²)
$A_{boundary}$	Area of channel wall (m ²)
a	Ellipse major axis length (m)
b	Ellipse minor axis length (m)
C	Specific heat of the coolant (J/kg·°C)
c_{Pp}	Specific heat of the part material (J/kg·°C)
c_{tool}	Specific heat of tool material (J/kg·°C)
d	Minimum cavity to cooling channel distance (m)
d_h	Hydraulic diameter (m)
D_{max}	Maximum diameter of the cooling channel (m)
h	Convective heat transfer coefficient (W/m ² ·K)
$k_{coolant}$	Thermal conductivity of fluid (W/m·K)
L	Characteristic length (m)
l	Length of pipe segment (m)
\dot{m}	Mass flow rate (kg/s)
m_p	Mass of molded part (kg)
Nu	Nusselt number
P	Perimeter (m)
\dot{Q}	Rate of heat transfer (W)
\dot{Q}_c	Heat removal rate of a cooling system (W)
Q_T	Heat removed by a cooling system (J)
R_a	Averaged surface roughness (μm)
R_z	Mean roughness depth (μm)
Re	Reynold's number
s	Thicket section of part (m)
t_{ce}	Minimum time to cool a part region (s)
T_{fluid}	Temperature of the solid channel surface (K)

T_{solid}	Temperature of the fluid channel surface (K)
T_{in}	Temperature of fluid at the inlet (K)
T_{out}	Temperature of fluid at the outlet (K)
T_i	Plastic injection temperature (K)
T_e	Plastic ejection temperature (K)
T_w	Wall temperature of cavity (K)
T_c	Approximate coolant material (K)
T_m	Melt temperature (K)
v	Fluid velocity (m/s)
ν	Kinematic viscosity (m ² /s)
\dot{V}_c	Volumetric flow rate of coolant (m ³ /s)
α_p	Thermal diffusivity (m ² /s)
Δp_f	Pressure loss across channel (Pa)
ΔT_c	Temperature change across a cooling channel (K)
α	Thermal diffusivity (m ² /s),
ε	Roughness of pipe for relative roughness (μm)
λ	Pipe friction factor
μ	Dynamic viscosity (kg/m·s)
ρ	Fluid/coolant density (kg/m ³)
ρ_{tool}	Density of tool material (kg/m ³)
τ_{cycle}	Mold cycle time (s)

Statement of the Problem

Injection molding

During the injection mold cycle, molten plastic is injected into an injection mold tool. The plastic fills the cavity of the mold as a large injection pressure forces the plastic into vacant regions so that the part is fully formed. The plastic cools as heat is absorbed by the mold. The part is allowed to solidify under a holding pressure until all part features are sufficiently cooled. Lastly, the mold core and cavity separate so that part can be ejected. The cooling phase is typically the longest part of the injection mold cycle, typically 50-75% of cycle time [1]. To reduce cooling time and remove the heat from the molten plastic, molds are cooled by running coolant through internal channels. This network of cooling channels is called a *cooling circuit*. Heat is conducted through the mold body, and then transferred to the cooling channels through convection. The design of the cooling circuit has a large influence on the cooling time required.

Conventionally, injection mold tooling is typically fabricated by machining tool steel. The fabrication of molds complicates the design optimization of cooling systems. Conventional injection mold cooling channels are made by various machining processes: wire EDM; milling; and most commonly, drilling and boring. A network of drilled holes is then routed and plugged on the ends to form an internal cooling circuit. Though cooling performance is the primary objective of cooling system design, the design is constrained by the geometry of the mold: the part cavity, ejector pin systems, and other action in the mold. In addition, the process limitations of drilling restrict the potential geometry of the cooling circuit in two distinct ways. Firstly, a section of the cooling circuit must typically be machined along a single linear axis. Common processes include drilling and reaming. For molded parts with curvature, this prevents the cooling circuit from

maintaining a consistent distance from the cavity. *Conformal cooling*, where a cooling channel follows the shape of the mold cavity to maintain uniform cooling, is not achievable. Secondly, the cross-section of the channel must be circular with drilled channels. Assuming equal area, circles have the least perimeter. For a cooling channel, this minimizes the surface area where heat is exchanged.

Thermal pins, baffles, and other solutions are also currently used to decrease the cooling time of a mold. Complex fabrication and assembly of CNC-machined cooling circuits is also an option. Generally, these methods are less common and add complexity to mold design and fabrication. For this reason, metal additive manufacturing processes can be considered.

Alternative Applications

Other industrial tool processes that require cooling also employ the practice of internal cooling systems, as seen in die-casting. Cooling channel fabrication methods described in later chapters may be relevant to all casting or molding processes where absorption of heat from the mold is desired. Among other factors, the coolant, temperature ranges, flow requirements, and other key aspects of the process may vary. However, the methods of designing and fabricating various cooling systems are similar through traditional toolmaking approaches.

Heat exchangers use the flow of one fluid to heat or cool another fluid. This typically involves the flow of fluid through a pipe that runs through or beside another fluid mass. This is similar to the method used in injection mold cooling systems, but there is a convective boundary on both sides of the pipe wall for each fluid.

Moon et al. evaluated the performance of micro-heat pipes in electronics cooling applications. The cooling performance was studied for copper pipes of different cross sections, seen in Figure 1 [2].

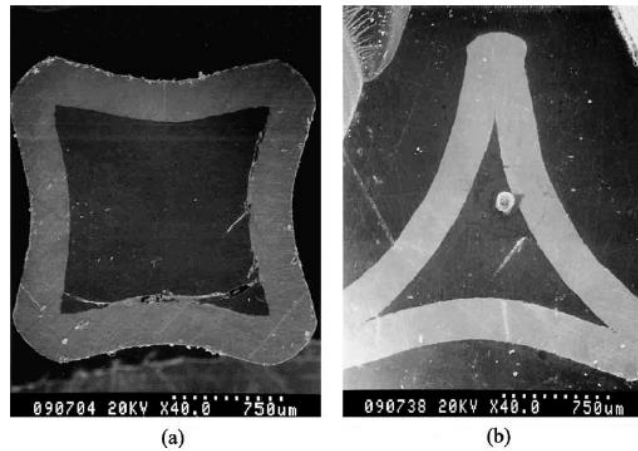


Figure 1: Experimental cross-sections of a micro-heat pipe.

One of the greatest technical challenges for using additive manufacturing to produce internal cooling channels is the complex relationship between surface roughness and cooling performance. The surface roughness is highly dependent on build orientation and other conditions. Ventola et al. (2014) demonstrated the convective and conductive cooling properties of DMLS-fabricated surfaces for the purpose of air-cooling electronics [3]. Further research should be conducted so that the cooling characteristics of additively manufactured parts can be more accurately estimated as a consequence of part design, powder material selection, and build parameters.

Research Objectives

The purpose of this investigation is to determine if additively manufactured cooling systems can be created to increase the performance of a cooling channel. Two objectives were identified:

- (a) Increase the rate of heat transfer from the parent material into the coolant within the channel.

(b) Reduce the coolant flow rate needed to achieve the same rate of heat transfer.

In this study, 316L stainless steel blocks with internal cooling channels were tested. Each block was created with various parent material conditions, channel wall surface finishing methods, and geometries of the internal cooling channel. In addition, computer simulations were performed which modeled the heat exchange of blocks with internal cooling channels.

References

- [1] R. Patukm, and L. Surange: “A review on cooling system design for performance enhancement of injection molding machine”. In International Conference on Global Trends in Engineer, Technology, and Management, 2016.
- [2] S. H. Moon, G. Hwang, S. C. Ko, and Y. T. Kim: “Experimental study on the thermal performance of micro-heat pipe with cross-section of polygon”, *Microelectronics Reliability*, 2004, vol. 44, no. 2, pp. 315-321.
- [3] L. Ventola, F. Robotti, M. Dialameh, F. Calignano, D. Manfredi, E. Chiavazzo, P. Asinari: “Rough surfaces with enhanced heat transfer for electronics cooling by direct metal laser sintering”, *International Journal of Heat and Mass Transfer*, vol. 75, 2014, pp. 58-74.

Advantages of Additive Manufacturing for Cooling Channels

Figure 2 shows visually how additively manufactured conformal cooling channels can improve mold design by reducing deviation in the cavity-to-cooling channel distance.

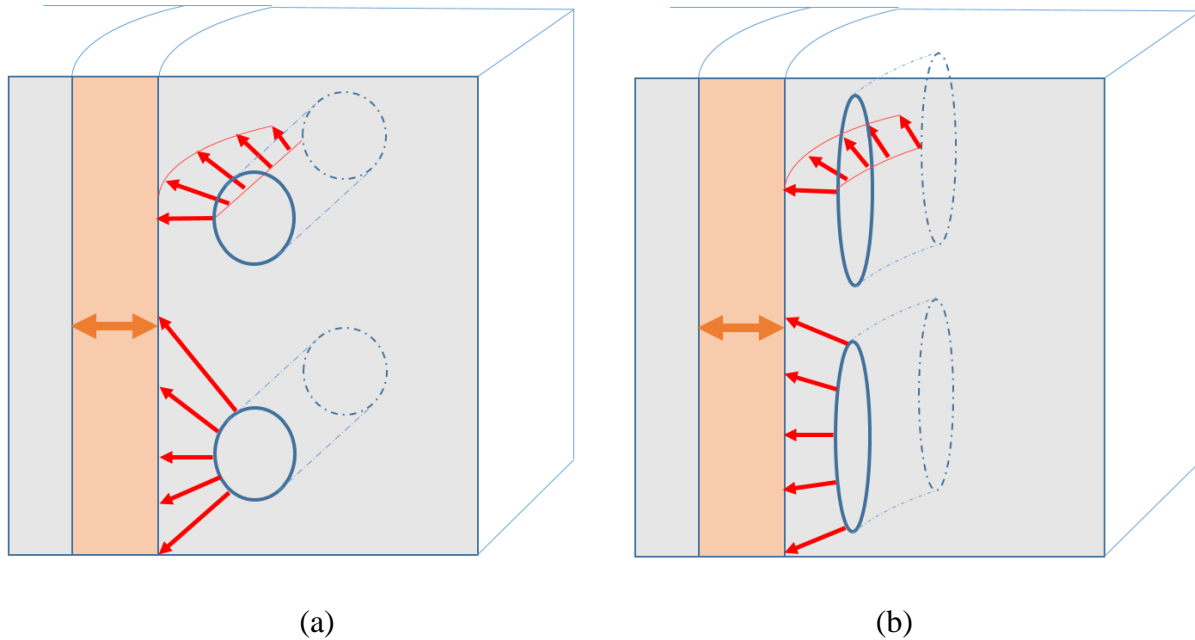


Figure 2: Visual comparison of the minimum cavity-to-cooling-channel distance for (a) conventionally cooled molds and (b) additively manufactured conformally cooled molds.

The cooling circuit path can be optimized because channels are not limited to a linear axis or a straight path. Among other situational benefits, a curved part cavity can have cooling channels that closely curve along the surface, decreasing the distance between the cooling channel and the part.

The cooling circuit is not limited to circular channels. The thermal and fluid properties of the cooling circuit can be varied by modifying the internal features and cross section. For example,

the cooling circuit can be modified to absorb heat efficiently from the hotspot of a mold. Another possible application is varying the cross-section of the cooling channel across a segment to facilitate uniform cooling across a non-uniform part region. This can also improve part quality by reducing residual stresses and reducing warpage [1]. Cooling performance is a consideration for mold design as an influence on the formation of defects such as sink marks, shrinkage, and flow lines.

Additive Manufacturing Definitions

The following terminology for additive manufacturing in this thesis is from the ISO/ASTM 52900:2015(E) standards [2]. 3D printing is the fabrication of objects through the deposition of material using a print head, nozzle, or another technology. Typically used in a non-technical context, synonymously with additive manufacturing. A 3D printer is a machine used for 3D printing. Additive manufacturing (AM) is the process of joining materials to make parts from 3D model data, usually layer upon layer, as opposed to subtractive and formative manufacturing technologies. Initial build orientation is orientation of the part as it is first placed in the build volume. Layers are the matter material laid out, or spread, to create a surface. The build surface is the area where material is added, normally on the last deposited layer which becomes the foundation upon which the next layer is formed. The first layer is often referred to as the build platform. The wiper or re-coater blade is the moving blade which distributes the next layer of powder material across the build surface. Directed energy deposition is the additive manufacturing process in which focused thermal energy is used to fuse materials by melting as they are being deposited. The powder bed is the part bed, or the build area in an additive manufacturing system in which feedstock is deposited and selectively fused by means of a heat source or bonded by means of an adhesive to build up parts. Powder bed fusion (PBF) is the additive

manufacturing process in which thermal energy selectively fuses regions of a powder bed. Laser sintering (LS) is the powder bed fusion process used to produce objects from powdered materials using one or more layers to selectively fuse or melt the particles at the surface, layer upon layer, in an enclosed chamber.

Additionally, several elements of fabrication using additive manufacturing will be defined by the author. The “build” of a LBPF-fabricated part is the physical process of creating the part using additive manufacturing. Support material is the material beneath the region undergoing fusion. This provides structural support for the current layer, which may be molten. Build angle is the angle at which the body of support material is built beneath the region undergoing fusion. A vertical surface that is fully supported underneath the fused material will have a build angle of 0. A horizontal surface with no rigid supports underneath has a build angle of -90, and is completely unsupported. Similarly, a horizontal surface with a rigid part body underneath will have a 90 degree build angle. An example part is shown in Figure 3.

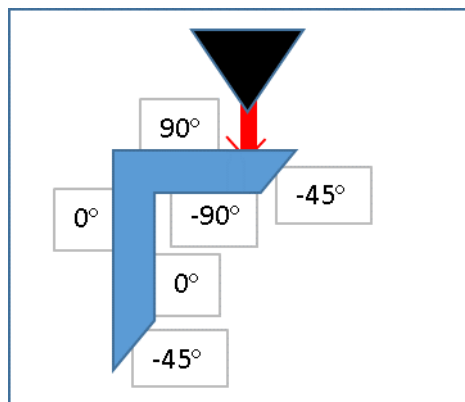


Figure 3: Example build angles of various surfaces.

Various “types” of powder bed fusion are available. Common process terminology includes direct metal laser sintering (DMLS), selective laser melting (SLM), and electron beam

melting. Historical differences have previously separated SLM and DMLS processes. Complete melting of metal materials was not always achievable; traditional powdered metal sintering involved using a mold and heat and/or pressure.

For the purposes of this thesis, the powder bed fusion processes will be differentiated. Electron beam melting (EBM) uses the thermal energy of an electron beam to join material. Laser powder bed fusion (LPBF) uses the thermal energy of a laser to join material. This includes DMLS and SLM processes. Direct metal laser sintering (DMLS) uses the thermal energy of a high-power-density laser to join material. The DMLS process does not apply enough thermal energy to fully melt or liquefy the metal powder. Only enough thermal energy is applied to fuse particles together. The word sintering is largely a misnomer as modern laser powder bed processes typically involve full or partial melting. Most modern laser powder bed fusion machines are capable of both melting and sintering of material. Selective laser melting (SLM) uses the thermal energy of a high-power-density laser to join material. The SLM process is capable of fully melting metals, and typical LPBF machines will be capable of selective laser melting. Laser powder bed fusion (DMLS and SLM) processes will be the focus of this thesis.

History of Additive Manufacturing for Conformal Cooling

The use of additive manufacturing with metal powder, commonly known as metal 3D-printing, has been critical for the development of conformal cooling. Currently, laser powder bed fusion processes have been proven to improve mold cooling performance compared to conventional molds in certain case studies. Typically, these studies are based on experimental findings by comparing simulated or physical mold tool studies. Generally, the heating and cooling properties of an individual cooling channel are not measured independently of the surrounding

mold. Often, the primary experimental output is the change in mold cooling time, as opposed to the rate of heat transfer for a cooling channel. Therefore, the direct knowledge is not always captured for how a cooling channel performs independently of mold geometry or the advantages of conformal cooling.

In one study for an injection mold tool, Schmidt et al. [3] demonstrated that additively manufactured conformal cooling methods reduced cycle times by 19-20% over fully machined parts.

Altaf et al. [4] reduced cooling time by about 18% by modifying the cross section of a cooling channel to decrease average distance from the cavity to the cooling channel. The experimental molds used by Altaf et al. are seen in Figure 4.

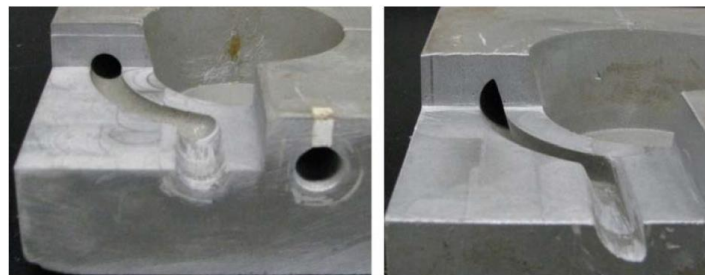


Figure 4: Cast aluminum molds, used to assess cooling performance of a semi-circular cooling channel.

Currently, between the vast array of engineering resources and the extensive practical knowledge for traditionally machined molds, the nature of conventional injection mold systems is well documented and understood. CAE software such as C-Mold, MOLDFLOW, and Solidworks Plastics can be used to design tools for injection molding. Mold layouts can be analyzed, which include: cooling circuits, mold action, cavities, sprues, runners, gates, and other mold elements. Simulation is used to model and predict thermal and mechanical behavior of a particular mold design. This gives mold designers the ability to predict cycle times, part warpage, and requirements

for the feed and coolant systems. Perhaps the most difficult part of implementing conformal cooling into injection mold tools is the uncertainty of the process compared to the well-understood nature of traditional machining.

Flow of Coolant through a Channel

For effective cooling, the flow should be highly turbulent. Reynolds number, Re , is non-dimensional ratio of inertial forces to viscous forces for a fluid. For fully developed flow in a pipe, laminar flow occurs when $Re < 2300$, and turbulent flow occurs when $Re > 2900$. Equation 1 defines the Reynolds number as:

$$Re = \frac{\rho v d_h}{\mu} = \frac{v d_h}{\nu} \quad \text{Equation 1}$$

where ρ is the fluid density (kg/m^3), v is the fluid velocity (m/s), d_h is the hydraulic diameter of the channel (m), μ is the dynamic viscosity of the fluid ($\text{kg/m}\cdot\text{s}$), ν is the kinematic viscosity of the fluid (m^2/s).

Darcy–Weisbach Equation

The flow of coolant through a circular channel or pipe is established with Equation 2:

$$\Delta p_f = \lambda \frac{l}{d_h} \frac{\rho v^2}{2} \quad \text{Equation 2}$$

where Δp_f is the pressure loss across the section of channel (Pa), λ is the Darcy pipe friction factor, l is the length of the segment (m), d_h is the hydraulic diameter of the channel (m), ρ is fluid density (kg/m^3), and v is fluid velocity (m/s).

Hydraulic Diameter

The hydraulic diameter for circular channels is equal to the inner channel diameter. As a generic equation, hydraulic diameter d_h (m) is calculated in Equation 3 from the channel cross-sectional area A and the boundary perimeter P :

$$d_h = 4 \frac{A}{P}$$
$$d_h = 4 \frac{[\pi ab]}{\left[2\pi \sqrt{\frac{a^2 + b^2}{2}} \right]} \quad \text{Equation 3}$$
$$d_h = 2 \frac{ab}{\sqrt{\frac{a^2 + b^2}{2}}}$$

So, for an ellipse, the major axis length a (half of the maximum width, m) and the minor axis length b (half of the height, m) can be used to determine hydraulic diameter of ellipses.

For an ellipse, the equation for a perimeter is a calculation of an infinite series. For simplicity, the Ramanujan approximation seen in Equation 4 was used.

$$i = \frac{(a - b)^2}{(a + b)^2} \quad \text{Equation 4}$$

$$P \approx \pi(a + b) \left(1 + \frac{3i}{10 + \sqrt{4 - 3i}} \right)$$

Pipe Friction Factor

The Darcy pipe friction factor is dependent on surface roughness of the channel wall, and varies by material and process selection. For laminar flows, the friction factor is calculated by

dividing 64 by the Reynold's number, known as the Hagen-Poiseuille equation. For turbulent flow, the relationship is complex.

From experimental results, Cheng [5] developed equations for friction factor λ for conventional, drilled channels with Equation 5. Equation 6 shows friction factors for SLM fabricated channels:

$$\lambda = 0.3164 Re^{-0.25}, 4000 < Re < 100,000 \quad \text{Equation 5}$$

$$\lambda = \left[1.14 - 2 \log_{10} \left(\frac{\varepsilon}{d_h} + \frac{21.25}{Re^{0.9}} \right) \right]^{-2} \quad \text{Equation 6}$$

In Equation 6, ε/d_h is the relative roughness of the pipe. Other equations exist for other geometries and intensities of turbulent flow.

Moody Chart

The relationship between surface roughness, friction factor, and Reynold's number is visually represented in a moody chart, shown in Figure 5 [6]. For cooling channels with larger surface roughness values, the mass flow rate will be lower where the pressure drop is equal. While the Moody chart is determined through extensive experimental data, a complete theoretical determination for pipe flow has not been proposed.

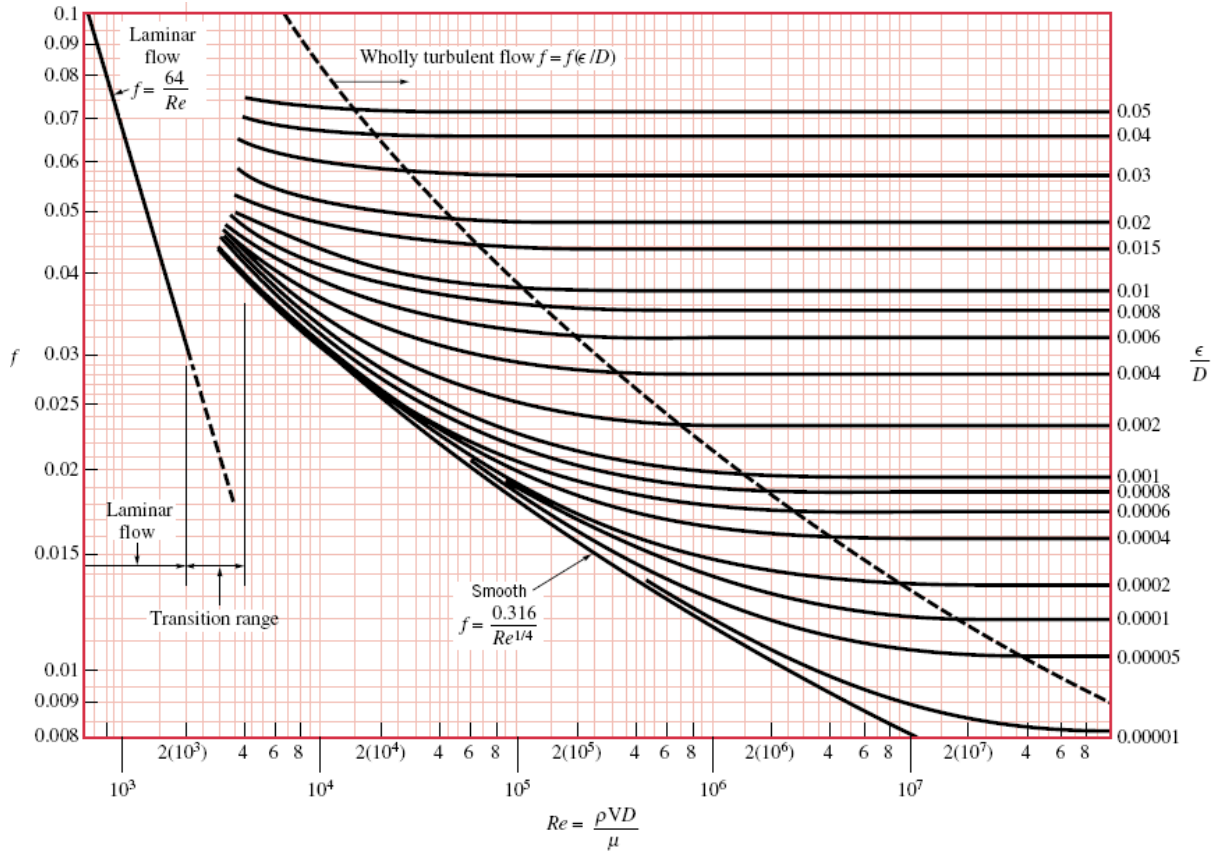


Figure 5: Moody chart.

Proposed Models for Friction Turbulence

Historically, the mathematical modeling of turbulent flow is an issue for the development of accurate theoretical models. Classical relationships between roughness and turbulence were determined through experimental data. Figure 6: Experimental data in Nikuradse's experimental friction-turbulence model. Figure 6 shows Nikuradse's data from 1950 that shows the friction coefficient of a pipe wall at various levels of turbulence [7].

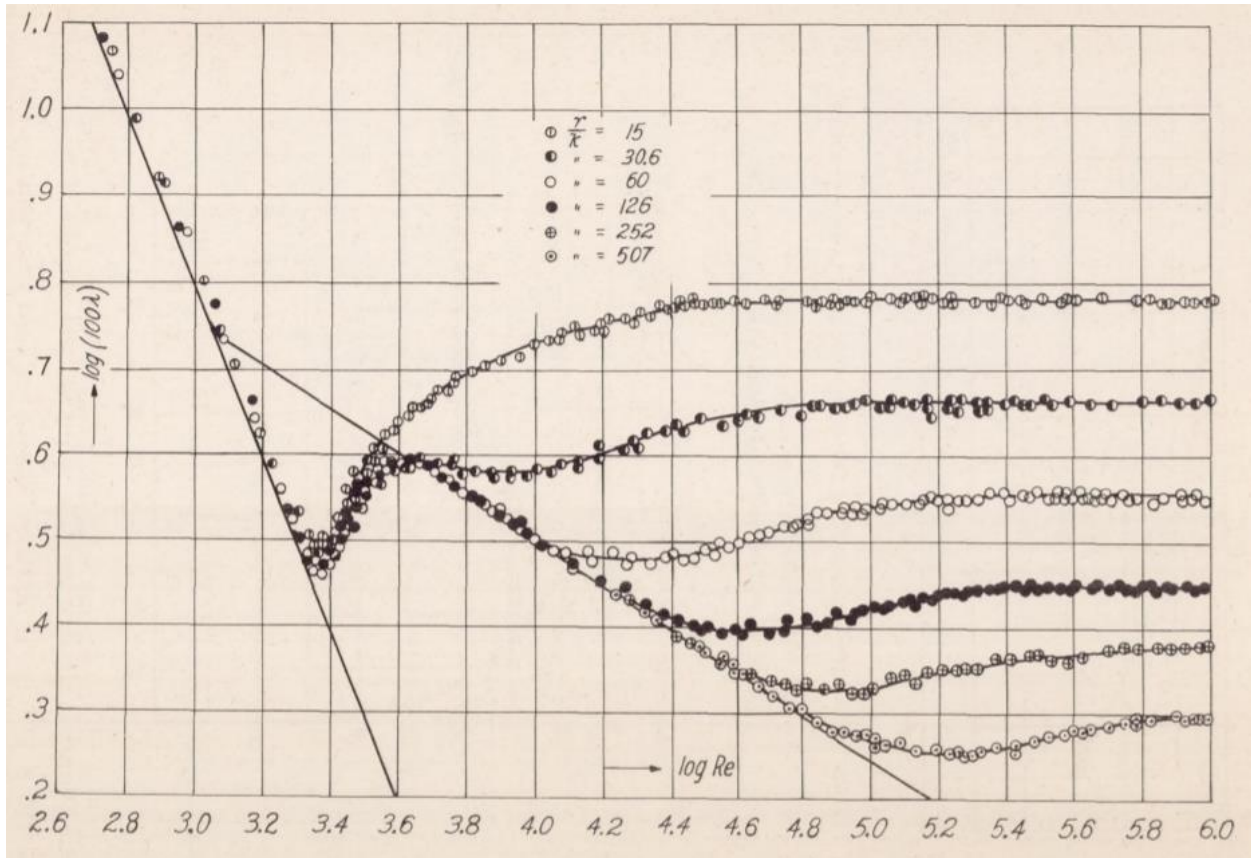


Figure 6: Experimental data in Nikuradse's experimental friction-turbulence model.

Gioia & Chakraborty examined classical models of experimental turbulence. Modern models of theoretical turbulent flow often combine several experimental models that are weighted across a range of flow conditions. One such example is seen in Figure 7 [8].

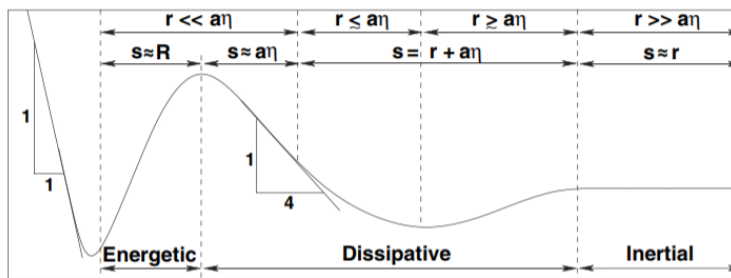


Figure 7: A relationship schematic along a Nikuradse Curve across the spectrum of turbulent energy, roughness, thickness of viscous layer, and dominant eddie size.

Model of Cooling for a Cooling Channel

Overall Rate of Convection Heat Transfer

At the walls of the channel, an overall heat transfer rate \dot{Q} is expressed in Equation 7, where h is the convective heat transfer coefficient ($\text{W}/\text{m}^2\text{K}$), $A_{boundary}$ is the total surface area at the walls of the channel (m^2), and T_{solid} and T_{fluid} are the temperature of the solid surface and the fluid, respectively (K). The convective heat transfer coefficient h is dependent on material properties which vary between materials and manufacturing processes.

$$\dot{Q} = hA_{boundary}(T_{solid} - T_{fluid}) \quad \text{Equation 7}$$

The rate of heat transfer \dot{Q} into the coolant from the surrounding solid body can be experimentally calculated with Equation 8 where c is the specific heat of the coolant ($\text{J}/\text{kg}^\circ\text{C}$), \dot{m} is the mass flow rate (kg/s), and T_{in} and T_{out} are coolant temperatures at the inlet and outlet, respectively (K).

$$\dot{Q} = c\dot{m}(T_{out} - T_{in}) \quad \text{Equation 8}$$

Because the ultimate goal is to absorb heat from surroundings as quickly as possible, the rate of heat transfer is the primary cooling performance indicator for a cooling circuit segment.

Convection Cooling and the Nusselt Number

The nusselt number is the ratio of convective heat transfer to conductive heat transfer across a boundary. The conductive component is determined as the heat transfer with a stagnant fluid.

Greater turbulence increases the convective heat transfer, which results in a greater nusselt number.

The relationship for the nusselt number Nu is given in Equation 9.

$$Nu = \frac{\text{Convective heat transfer}}{\text{Conductive heat transfer}} = \frac{h}{k_{coolant}/L} = \frac{hD_h}{k_{coolant}} \quad \text{Equation 9}$$

where $k_{coolant}$ is the thermal conductivity of the cooling fluid (W/m·K) and L is the characteristic length of the channel. The characteristic length can be defined by complex shapes as the volume of the cooling channel divided by the surface area of the channel walls. A Nusselt number of $Nu=1$ for a fluid layer indicates that heat is transferred entirely by conduction.

Ventola et al. (2014) determined that an increased surface roughness enhanced convective heat transfer for air-cooled DMLS part surfaces [9]. The nusselt number was determined at various levels of turbulence and compared between samples, as seen in Figure 8.

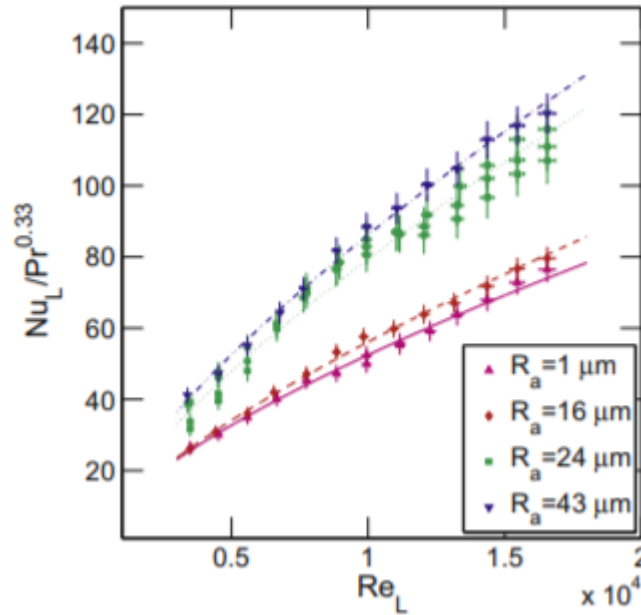


Figure 8: Nusselt number vs. Reynolds number for air-cooled DMLS surfaces of various roughnesses. The $R_a=1\mu m$ sample was milled post-build for comparison.

Approximations from Previous Research

Because the injection mold cycle causes a cyclical change in mold temperature, the heat absorption of the cooling system can be expressed in relation to the injection mold cycle. Neglecting the heat transfer to the surrounding environment, Menges et al. [10] defines a one-dimensional rate of heat transfer for an injection mold cooling system in Equation 10:

$$\dot{Q}_c = \frac{Q_T}{t_{ce}} = \frac{m_p c_{Pp} (T_i - T_e)}{t_{ce}} \quad \text{Equation 10}$$

where \dot{Q}_c is the heat removal rate of the cooling system (W), Q_T is the total heat removed by the cooling system (J), and t_{ce} is the minimum time required to cool a particular part region (s). Equation 10 differs from Equation 8 because the rate of heat transfer for the cooling system is driven by the part cooling cycle. The total heat absorbed is obtained by determining the part mass m_p (kg), the specific heat capacity c_{Pp} of the part material (J/kg $^{\circ}$ C), and the temperatures for injection and ejection, T_i and T_e (K). Since different part sections will have different cooling times for different part thicknesses, the thickest part section s (m) and the wall temperature T_w (K) are used to find the cooling time. Assuming that a circular cooling channel is close enough to the mold wall that T_w is roughly equal to coolant temperature and the mold has thermal diffusivity of α (m 2 /s), Menges et al. [10] calculated the longest part cooling time in Equation 11 and recommended that the coolant temperature ΔT_c increases 3-5 degrees Celsius or less.

$$t_{ce} = \frac{s^2}{\pi^2 \alpha} \ln \left(\frac{4 T_i - T_w}{\pi T_e - T_w} \right) \quad \text{Equation 11}$$

In order to adequately cool the system, sufficient amounts of coolant should flow. Menges et al. [10] obtain \dot{V}_c (m³/s), the required volumetric flow rate of the coolant, in Equation 12 as:

$$\dot{V}_c = \frac{\dot{Q}_c}{\Delta T_c \rho C} \quad \text{Equation 12}$$

where ρ is the coolant density (kg/m³), and C is the specific heat capacity for the coolant (J/kg·°C). For conventional mold design, the maximum diameter of the cooling channel D_{max} is seen in Equation 13.

$$D_{max} < \frac{4\rho\dot{V}_c}{\pi\mu Re} \quad \text{Equation 13}$$

For smaller channels, a constraint is the larger pressure drop across the cooling channel. For injection mold cooling systems, the intended Reynolds number Re is intended to be large. Reynolds number values of over 10,000 are desirable, but the main requirement is to ensure that the turbulent flow of coolant is adequate.

Conduction of a Cooling Cell

Figure 9: A cooling cell for a circular cooling channel. Figure 9 shows the cross section of a cooling cell, including the points where distance from the cooling channel is minimum and maximum.

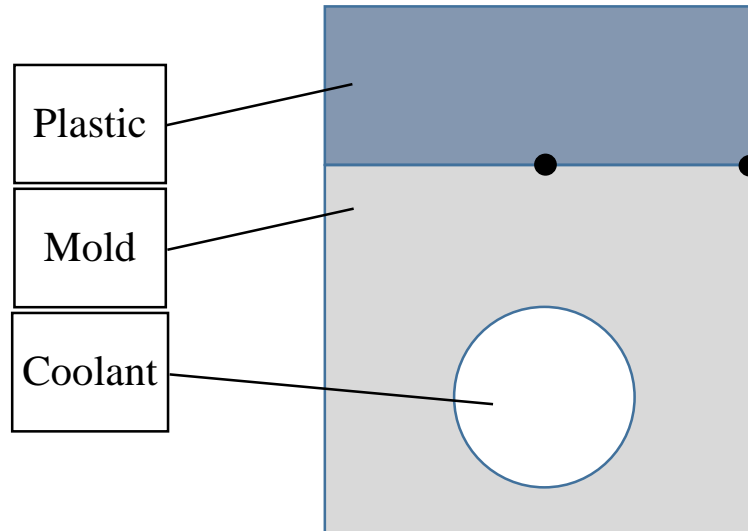


Figure 9: A cooling cell for a circular cooling channel.

Sachs et al. (2000) proposed a 1-dimensional heat flow model for the mold material. Note that in this equation, there is no local cooling from coolant. Under this condition, heat flow per unit area into the mold can be modeled in Equation 14. Assuming the tool material between the surface and channel is an average of the melt temperature T_m and the coolant temperature T_c (K), heat flow into the tool per unit area is:

$$\rho_{tool}c_{tool}d\left(\frac{T_m + T_c}{2} - T_c\right) = \rho_{tool}c_{tool}d\frac{T_m + T_c}{2} \quad \text{Equation 14}$$

where ρ_{tool} and c_{tool} are the density and specific heat of the tool material (J/kg $^{\circ}$ C), and the closest distance to the cooling channel is d (m).

It was found that in order to cool the mold sufficiently, it must be significantly less than the cycle time. In order for conformal cooling systems to provide enough cooling, this condition limits the distance d from the mold surface to the closest part of the cooling channel. This relationship is seen in Equation 15 [11]. τ_{cycle} is the cycle time (s).

$$d < \sqrt{\frac{k\tau_{cycle}}{\rho_{tool}c_{p_tool}}} = \sqrt{\alpha\tau_{cycle}} \quad \text{Equation 15}$$

SLM Factors and Existing Case Studies

Material Characteristics of Laser Powder Bed Parts

The functional characteristics of powder metal parts can be affected by processing parameters and powder material. Yadroitsev suggests that over 130 parameters may affect part quality [4]. Many of the key factors affect the application of thermal energy from the laser to fuse the powder material. Subsequently, these factors drive functional effects on part density, structural behavior, and ability to conduct heat energy. The morphology of surfaces is also heavily influenced by process parameters.

Table 1 lists various process parameters that are generally considered to have notable effect on the thermal properties of the part.

Table 1: Key process parameters for laser powder bed fusion of metals.

Parameter	Unit	Citation
Laser power	W	[12]
Laser speed	mm/s	[12]
Hatch spacing	mm	[12,13]
Powder layer thickness	mm	[12,13]
Powder size distribution	μm	[12]
Scanning strategy	n/a	[12,13]
Beam size	μm	[14]
Focal offset	mm	[12]
Atmospheric conditions	n/a	[13]
Powder bed temperature	°C	[12,13]

Thermal Conductivity of Machined versus Powdered Metals

Generally, the thermal properties of metals are not significantly affected by machining. Mold bodies typically exhibit comparable thermal characteristics as the original parent material.

Unlike machining processes, laser powder bed fusion processes can have significant effects on the thermal properties of powder parts. Historically, making parts that exhibit desirable material properties was a challenge to due to limitations in LBPF laser power. Technological developments have increased the power of lasers, allowing the production of parts with adequate layer fusion minimal porosity. Niendorf et al. (2013) list porosity, undesired microstructures, and high residual stress as the greatest technical limitations of SLM processes and discuss the laser power source as an input [15]. Currently, only certain materials such as 316L stainless steel have been extensively

demonstrated to successfully exhibit relative densities near 100%. Kamath et al. (2013) describes a keyhole-mode of laser melting in the powder bed, and the fusion of that molten material to underlying layers [14]. In keyhole-mode laser melting, the density of power from the laser beam is great enough to evaporate the metal and form plasma. This creates a vapor cavity that increases absorption of the laser. As a result, the laser beam reaches a greater depth than originally achievable with conduction alone. This cavity can collapse, leaving voids that reduce the relative density of the part. Thus, the processing parameters for laser powder bed fusion processes must be balanced so that a layer fully melts and fuses, but the melting is not sufficient to cause keyhole-mode melting.

Typical Input parameters for Injection Mold Cooling

Table 2 and Table 3 respectively show the system inputs and outputs for injection mold systems.

Table 2: Inputs for design of injection mold cooling systems.

Input	Unit	Description
Pressure in/out	Pa	Controlled by coolant supply.
Coolant temperature in	°C	Controlled by coolant supply or inlet temperature.
Cooling system path	n/a	Pathway affects cooling function and coolant flow.
Channel cross-section or diameter	mm ² , mm	Changes the flow rate. Also, greater perimeters increase the area where convective heat transfer can occur. Thus, greater area increases the rate of heat transfer in addition to increased flow.

Table 3: Outputs for design of injection mold cooling systems.

Output	Unit	Description
Coolant pressure drop	Pa	There is typically a desirable range of pressure drop across the cooling system. Pressure drop can be considered across the entire system, or only a segment of the cooling circuit.
Coolant temperature rise	°C	It is encouraged to design cooling circuits where the temperature increase is small (generally within a few degrees Celsius). Temperature rise can be considered across the entire system, or only a segment of the cooling circuit.
Rate of heat transfer	W	Since the objective is to remove heat from the cavity of the mold as quickly as possible, the average rate of heat transfer across an injection molding cycle should be maximized.
Cooling time	s	The time between injection holding and part ejection. In practice, cooling time is a process parameter. However, cooling time should be minimized as much as possible.

Surface Roughness of Channel Wall

Achieving internal walls with low surface roughness for the cooling system is a challenge for mold fabricators. In the traditional material removal processes of milling, drilling, and boring, careful selection is critical for machining parameters such as cutting speed and feed rate.

Surface roughness of the interior channel walls affects the flow of the pipe by increasing the friction factor. Post processing is used to reduce surface roughness of parts beyond what is

achievable with additive manufacturing. Machining, heat treatment, and various surface polishing methods are used to smoothen external part features and remove unmolten particles. Still, one limitation of laser powder bed fusion based processes for metals is that achieving a surface roughness comparable to a machined part is either difficult or unfeasible. Not all methods of reducing surface roughness are physically possible for applications that require the smoothing of internal features. Some procedures currently used are abrasive flow machining, sandblasting, and post-build heat treatments. Without post-processing, Kruth et al. (2010) demonstrated that surface quality can be improved by using the laser during the build to re-melt surfaces [16], as seen in Figure 10.

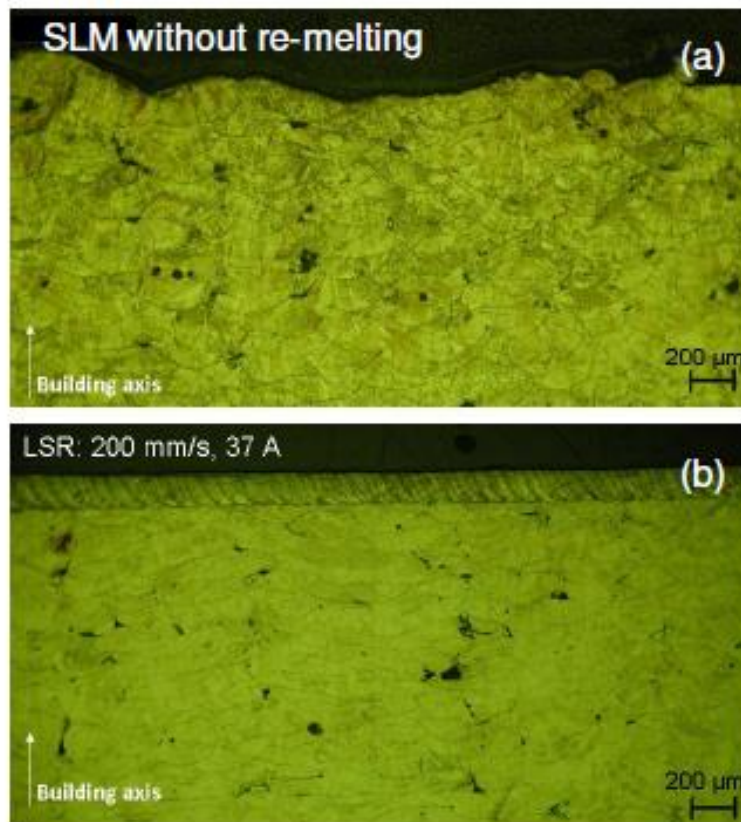


Figure 10: Surface morphology of 316L stainless steel, fabricated with SLM. (a) shows a surface without re-melting. (b) shows the surface of a re-molten part.

For external features, removable supports can be made underneath the part to maintain rigidity during fabrication. One challenge of successfully fabricating internal features in laser powder bed fusion processes is that unsupported faces during the build result in rougher surfaces, unmolten material, or dimensional warpage due to thermal stress. Figure 11 shows some geometries that may be difficult to build [17]. Unsupported faces that are relatively horizontal or large in size should be avoided during build.

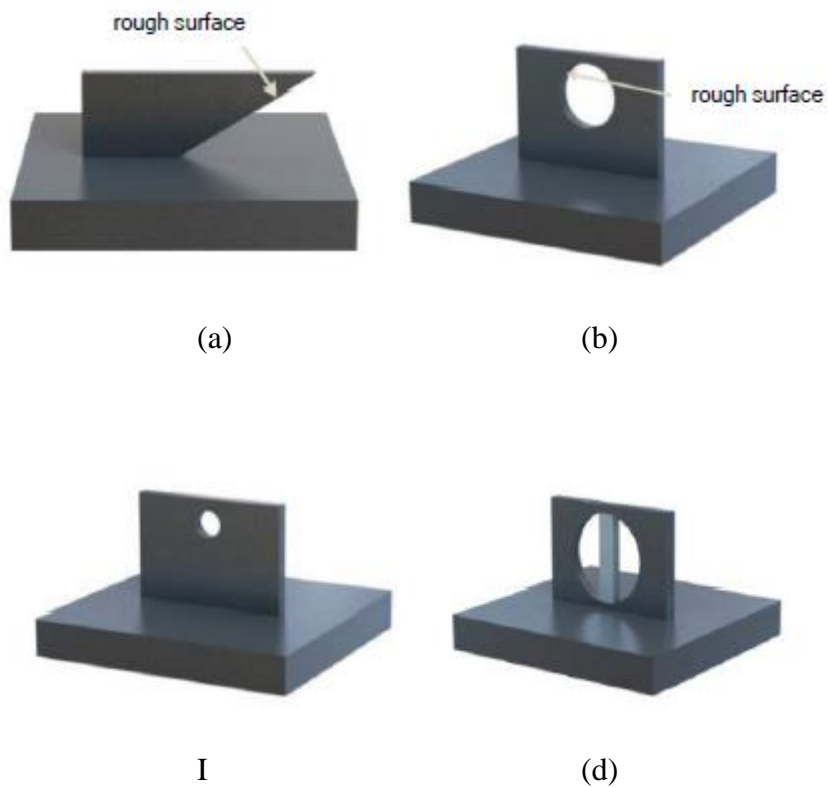


Figure 11: Internal feature design guide for EOS M290 [17]. (a) and (b) depict rough surfaces for unsupported faces. (c) shows a hole smaller than 6mm – ideally small enough to not require supports. (d) shows a larger hole where support structures are used to support the feature.

Process Recommendations for Laser Powder Bed Fusion Processes

Build orientation and material support considerations

Channels that are built as vertical extrusions, such as those seen in Figure 12, will have smoother surfaces than channels built horizontally. This is because there is always supporting material underneath the layer of powder; for straight extruded parts, the angle of support will always be 0 degrees. For shorter parts, this is ideal. However, for longer parts, vertical builds will require significant amounts of powder material to reach the required height. This can increase the cost-per-build, and increase build time as time is spent adding more powder to the bed.

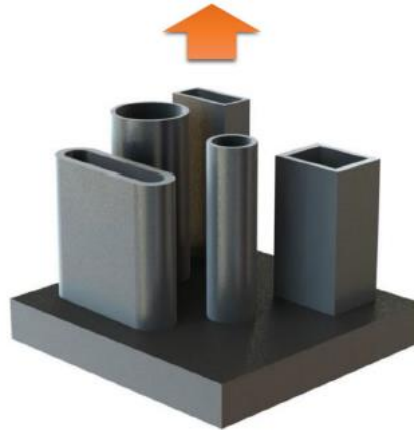


Figure 12: Vertical build orientations provide the best surface finish [17].

For complex tools, different sections of the cooling circuit may require horizontal or vertical build orientations. The surface roughness of internal cooling channels built vertically will be consistent because the entire channel is supported. For horizontally built cooling channels, the unsupported top surface will be the roughest region. Since horizontal extrusions are the most challenging geometry for laser powder bed processes, optimization of horizontal extrusions will be the focus of this experiment. In practice, an additively manufactured cooling circuit will have a

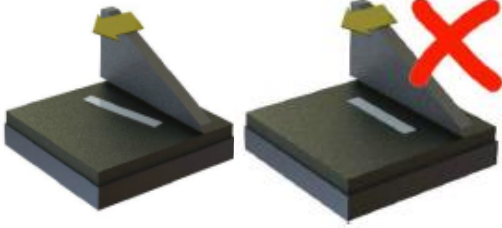
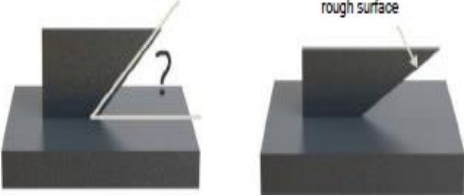
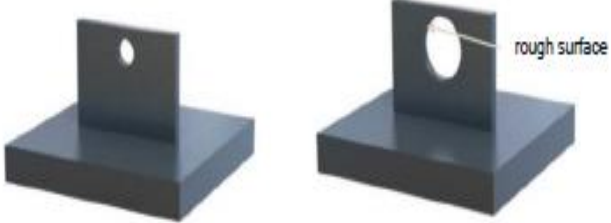
combination of horizontally and vertically built channels. For this reason, build orientation should be considered as a design element.

Experimental Parameters

Cooling channel geometry was chosen from process recommendations from the machine manufacturer. It is important to recognize the machine-specific capabilities and limitations of laser powder bed fusion processes. The machine used for this experiment is the EOS M 290.

Table 4 lists recommendations from the EOS DMLS design guide. In addition to manufacturer recommendations, geometry was based on reasonable dimensions for injection mold cooling channels. Typical conformal cooling systems have a pitch distance of 10mm, and diameter of 5mm. A typical minimum distance from the channel to mold wall is 3mm [18]. For other applications, such as cooling for electrical components, the overall dimensions may be larger or smaller.

Table 4: DMLS Design Recommendations for the EOS M 290.

Parameter	Description
Minimum wall thickness (mm)	For horizontally built features, wall sections should not be thinner than 1mm [17]. Finer detail is achievable for vertical builds, however. For the 316L stainless steel powder used, the minimum wall thickness is 0.3 to 0.4mm [19].
Minimum blade-to-face angle (°)	<p>For part faces parallel to the recoater blade, forceful collisions or part deformation can occur.</p> <p>5 degrees difference is recommended [17].</p> 
Minimum angle of self-support (°)	<p>For stainless steels, the minimum angle of self-supporting surfaces is approximately 30 degrees [17].</p> 
Hole size (mm)	<p>Holes of less than 6mm are ideal. Larger holes may need post-machining [17].</p> 
Estimated Surface Roughness (µm)	<p>As manufactured (no post-processing), $R_a=13\pm 5\mu\text{m}$; $R_z=80\pm 20\mu\text{m}$ [19].</p> <p>External faces can be polished to approximately $R_z=1\mu\text{m}$ [19].</p>

Based on the requirements of injection mold tooling and design considerations of additive manufacturing, a range of elliptical cooling channel geometries can be used. Table 5 shows the geometric properties of elliptical channels of the eight inch experimental channel length.

Table 5: Geometry of various elliptical cross-sections of equal area.

Height	6	7	8	9	10	12	14	16	18	20	mm
Width	6	5.143	4.5	4	3.6	3	2.571	2.25	2	1.8	mm
Ramanujan Perimeter	18.8	19.2	20.0	21.2	22.6	25.7	29.2	32.9	36.7	40.5	mm
Cross sectional area	28.274										mm ²
Channel length	203.2										mm
Channel wall surface area	3830	3899	4068	4304	4585	5229	5940	6687	7455	8237	mm ²
Channel volume	5745.345										mm ³
Hydraulic diameter and characteristic length	6.00	5.89	5.65	5.34	5.01	4.39	3.87	3.44	3.08	2.79	mm

Optimal cross sections for laser powder bed fusion processes

Elliptical cross sections were selected for this experiment for several performance and process related reasons. Firstly, it is easier to make ellipses w/ LPBF processes compared to circles of equal channel area (due to superior build support). Secondly, the transition between elliptical and circular regions can easily be influenced with lofted channel transition design. Lastly, even with equal convective cooling rates, greater surface area increases conduction cooling.

For additively manufactured cooling channels, the improvement in surface roughness will be demonstrated with two methods. The unsupported surface at the top of the cooling channel will have reduced area for ellipses with greater build height-to-width ratio. Also, for ellipses with

greater build height-to-width ratio, there is also reduced surface roughness in the supported region of the cooling channel surfaces.

Surface roughness as a function of build angle

It is established that pipes with greater surface roughness on the walls will result in greater turbulence. Without experimental data, determining how this will impact convection cooling performance is problematic.

Ellipses with a large major vertical axis, compared to circles, will have proportionally less surface roughness. This is because a greater portion of the channel wall will be vertically supported.

Unsupported features

Unsupported features at the top of horizontally built channels can have undesirable features such as unmolten particles that cannot easily be removed. With cooling systems that follow complex paths, these particles are difficult to remove. Ellipses built with the major axis vertically can minimize the region where these effects can occur. The adequate support of a surface can be difficult to define and can be dependent on part geometry, material, among other factors. For the purpose of this thesis, an unsupported surface will be defined as a surface with a build angle exceeding recommended values from EOS, the manufacturer of the machine that was used to fabricate the parts. The limit is 30° above the horizontal plane for a bottom surface [17]. Therefore, build angles from -90° to -60° will be considered unsupported. Figure 13 shows the range of unsupported perimeter for an elliptical channel. Table 6 shows the reduction in unsupported perimeter for various ellipses compared to a circular section.

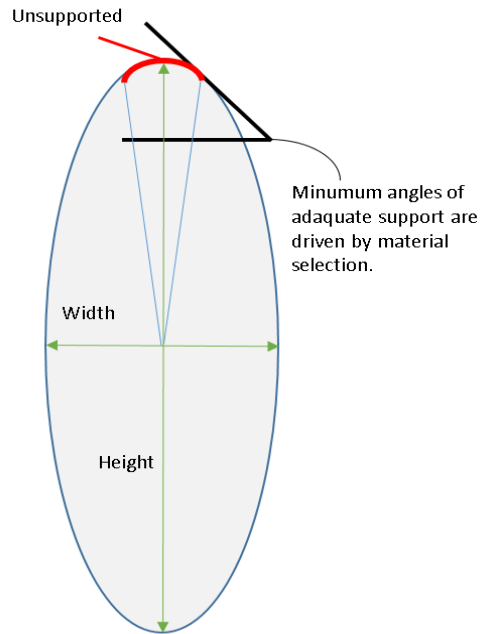


Figure 13: Unsupported feature, seen in the cross-section of a powdered metal cooling channel.

Table 6: Unsupported internal features of various elliptical channels of equal cross-sectional area.

Ellipse Build Height	6	7	8	9	10	12	14	16	18	20	mm
Ellipse Build Width	6	5.143	4.5	4	3.6	3	2.571	2.25	2	1.8	mm
Percent of perimeter unsupported by EOS design guide	16.7%	12.8%	10.0%	8.0%	6.5%	4.6%	3.4%	2.6%	2.0%	1.7%	
Percent reduction compared to 6x6mm circle	0%	23%	40%	52%	61%	73%	80%	85%	88%	90%	

References

- [1] R. Patukm, and L. Surange: “A review on cooling system design for performance enhancement of injection molding machine”. In International Conference on Global Trends in Engineer, Technology, and Management, 2016.
- [2] ISO/ASTM Standard 52900 (2015). Standard terminology for additive manufacturing – general principles – terminology. ASTM International, West Conshohocken.
- [3] W. R. Schmidt, R. D. White, C. E. Bird, and J. V. Bak: “Conformal Cooling Versus Conventional Cooling: An Injection Molding Case Study With P-20 and 3DPTM-Processed Tooling”, MRS Proc., vol. 625, Cambridge Univ Press; 2000, p. 51.
- [4] K. Altaf, A.M. Abdul-Rani, and V. Raghavan: “Prototype Production and Experimental analysis for Circular and Profiled Conformal cooling Channels in Aluminium Filled Epoxy Injection Mould Tools”, Rapid Prototyping Journal, 2016.
- [5] D. X. Cheng: “Handbook of mechanical design”, Chemical Engineering Press, Beijing, 2016.
- [6] I. Martin-Dominguez, M. Alarcón-Herrera, and J. Escobedo: “Determination of the Darcy Pipe Flow Friction Factor as a Routine in Visual Basic for MS Excel”, 2006.
- [7] Reprinted in English in J. Nikuradse, NACA Tech. Memo. 1292 (1950).
- [8] G. Gioia, and P. Chakraborty: “Turbulent Friction in Rough Pipes and the Energy Spectrum of the Phenomenological Theory”. Physical review letters, 2006, vol. 96, 044502.
- [9] L. Ventola, F. Robotti, M. Dialameh, F. Calignano, D. Manfredi, E. Chiavazzo, P. Asinari: “Rough surfaces with enhanced heat transfer for electronics cooling by direct metal laser sintering”, International Journal of Heat and Mass Transfer, vol. 75, 2014, pp. 58-74.
- [10] G. Menges, W. Michaeli, P. Mohren: “How to make injection molds”. Carl Hanser GmbH, München, 2001.

- [11] E. Sachs, E. Wylonis, S. Allen, M. Cima, and H Guo: “Production of injection molding tooling with conformal cooling channels using the three dimensional printing process”, *Polymer Engineering and Science*, 2000, vol. 40, pp. 1232-1247.
- [12] M. Mazur, P. Brincat, M. Leary, and M. Brandt: “Numerical and Experimental Evaluation of a Conformally Cooled H13 Steel Injection Mould Manufactured with Selective Laser Melting”, *The International Journal of Advanced Manufacturing Technology*, 2017, vol. 93, no. 1-4, pp. 881-900.
- [13] Yadroitsev, I. (2009). *Selective laser melting : direct manufacturing of 3D-objects by selective laser melting of metal powders*. LAP Lambert Academic Publishing.
- [14] C. Kamath, B. El-dasher, G. F. Gallegos, W. E. King, and A. Sisto: “Density of Additively-Manufactured, 316L SS Parts Using Laser Powder-Bed Fusion at Powers Up to 400W”, United States: N. p., 2013.
- [15] T. Niendorf, S. Leuders, A. Riemer, H. Richard, T. Tröster, and D. Schwarze: “Highly Anisotropic Steel Processed by Selective Laser Melting”. *Metallurgical and Materials Transactions*, 2013.
- [16] J. P. Kruth, M. Badrossamay, E. Yasa, J. Deckers, L. Thijs, and J. Humbeeck: “Part and material properties in selective laser melting of metals”. 16th International Symposium on Electromachining, ISEM 2010.
- [17] Design Guidelines for DMLS, Crucible Industrial Design.
- [18] X. Xu, E. Sachs, and S. Allen: “The design of conformal cooling channels in injection molding tooling”, *Polymer Engineering & Science*, 2001, vol. 41, pp.1265-1279.
- [19] EOS Stainless Steel 316L Material Datasheet, 2014.

- [20] S. H. Moon, G. Hwang, S. C. Ko, and Y. T. Kim: “Experimental study on the thermal performance of micro-heat pipe with cross-section of polygon”, *Microelectronics Reliability*, 2004, vol. 44, no. 2, pp. 315-321.
- [21] H. Brooks, and K. Brigden: “Design of conformal cooling layers with self-supporting lattices for additively manufactured tooling”. *Additive Manufacturing*, 2016.
- [22] Y. B. Guo, Y.K. Chou: “The determination of ploughing force and its influence on material properties in metal cutting”, *Journal of Materials Processing and Technology*, 2004, vol. 148, pp. 368–375.
- [23] M. Nasr, E.G. Ng, M.A. Elbestawi: “Modelling the effects of tool-edge radius on residual stresses when orthogonal cutting AISI 316L”, *International Journal of Machine Tools and Manufacture*, vol. 47, no. 2, 2007, pp. 401-411, ISSN 0890-6955.
- [24] J. Jiménez: “Turbulent flows over rough walls”. *Annual Review of Fluid Mechanics*, 2004, Vol. 36:173-196.

CHAPTER 3. EXPERIMENTAL INVESTIGATION AND COMPUTER SIMULATION

Inputs and Outputs

Fixed Inputs

Table 7 shows inputs for comparing elliptical cooling channels. The inlet pressures for simulation and experiment were set so that comparable flows could be observed between the simulation and experimental pipe lengths. The inlet pressure was chosen so that the inlet gauge pressure would be equivalent to 25 lb/in² pressure.

Table 7: Fixed inputs.

Parameter	Value	Unit	Used in simulation?	Used in experiment?
Inlet pressure	172369	Pa	No	Yes
Inlet pressure	33929	Pa	Yes	No
Outlet pressure	0	Pa	Yes	Yes
Inlet temperature	15	°C	Yes	Varies
Cross-sectional area of channel	28.27 (area of 6mm circle)	mm ²	Yes	Yes
Target heat source temperature	200	°C	Yes	Yes
Turbulent intensity of inlet and outlet	5.0	%	Yes	No
Turbulent viscosity ratio of inlet and outlet	10		Yes	No

Outputs

Table 8 shows the experimental outputs in comparing elliptical cooling channels

Table 8: Outputs in comparing elliptical cooling channels.

Parameter	Unit	Used in simulation?	Used in experiment?
Rate of heat transfer	W	Yes	Yes
Surface heat transfer coefficient	W/m ² K	Yes	No
Coolant flow rate (water)	kg/s	Yes	Yes
Turbulent intensity	%	Yes	No
Channel wall temperature	°C	Yes	No
Coolant temperature increase from inlet to outlet	°C	Yes	Yes

Simulation

Methodology

Simulation was used to compare various cooling channel cross-sections for overall cooling performance and flow properties. ANSYS Fluent was chosen as the software package for the simulation.

Model geometry

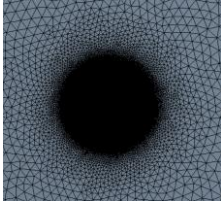
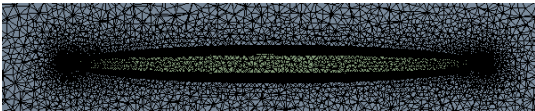
A 40mm length section of cooling channel was simulated, with a simplified model of the geometry of experimental pieces described in future sections. For the simulated model, no threaded

inlets were added. Additionally, no transitions to the experimental cross-sections were used. So, the inlet and outlets for the cooling channels are simply boundaries of the experimental cross-section, and flow at the boundaries is assumed to be normal to the plane of the inlet and outlet. 2 different channels of equal cross-sectional area were used, a 6x6mm circle and a 20x1.8mm ellipse. These values were chosen so the cross-sectional area of the cooling channels could be fixed at 28.274 mm², the equivalent of a 6mm diameter circle. However, the channel wall surface area is larger for elliptical channels with a larger width-to-height ratio as a result of the larger perimeter. Thus, the characteristic length is smaller for tighter elliptical sections.

Meshing of Simulated Model

A separate meshing strategy was employed for the 20x1.8mm ellipse. The tight elliptical corners could not be adequately simulated using a typical meshing strategy, so different meshing values were used. Table 9 shows the mesh parameters for the 6x6mm and 20x1.8mm channels.

Table 9: Mesh statistics.

Characteristic		6x6mm	20x1.8mm
Nodes		2370414	5989899
Elements		8098772	18451338
Orthogonal Quality	Min	0.121	0.163
	Max	0.998	0.998
	Average	0.783	0.776
	Std. Dev.	0.120	0.112
 6x6mm mesh section view.		 20x1.8mm mesh section view.	

Computation of Simulated Model

ANSYS Fluent was used by applying the model configuration seen in Table 10. In order to compare the results of the simulation and physical experiment, the pressure drop per unit length of the channel segment was set to be equal. To have comparable flow properties to the experiment, experimental flow rates for the conventionally machined and as-LPBF-fabricated elliptical channels were used to set inlet flow rates in the simulation.

Table 11 shows the bodies and boundaries of the model, including boundary conditions. For the simulated model, there were no additional transition features at the inlet and outlet for threaded connections – instead, fluid simply flows into the channel from the inlet and outlet parallel to the net direction of flow. The material properties in Table 12 were assigned from the ANSYS library. Solution methods are seen in Table 13.

Table 10: Model configuration for simulation.

Pressure-based solver		
Absolute Velocity Formulation		
Gravity (y-axis, -9.81 m/s ²)		
Viscous Model	Realizable k-epsilon	C2-Epsilon = 1.9
		TKE Prandtl Number = 1
		Energy Prandtl Number = 0.85
		Wall Prandtl Number = 0.85
	Enhanced wall treatment	Pressure gradient effects
		Thermal effects

Table 11: Bodies, boundaries, and conditions of CFD model.

Solid (mold)	Steel	
Heated surface	Fixed temperature	200 °C
	Steel	
Inlet	Gauge pressure	33929 Pa
	Hydraulic diameter	6x6mm: 6mm
		20x1.8mm: 2.7902mm
	Turbulent intensity	6.2%
	Fluid temperature	15 °C
	Inlet flow normal to boundary	
	Flow rate obtained from experimental measurements described in later sections.	
Outlet	Gauge pressure	0 Pa
	Hydraulic diameter	6x6mm: 6mm
		20x1.8mm: 2.7902mm
	Turbulent intensity	6.2%
	Backflow temperature	16 °C
	Backflow normal to boundary	
	Flow rate obtained from experimental measures described in later sections.	
Outer walls (excluding heat source)	No heat transfer	

Table 12: Material properties for simulation.

Water, liquid (coolant)	Density	998.2 kg/m ³
	Specific heat	4182 J/kg·°C
	Thermal Conductivity	0.6 W/m·°C
	Viscosity	0.001003 kg/m-s
Steel (mold material)	Density	8030 kg/m ³
	Specific heat	502.48 J/kg·°C
	Thermal conductivity	16.27 W/m·°C

Table 13: Solution methods.

Gradient	Least squares cell based
Pressure	Second order
Momentum	Second Order Upwind
Turbulent Kinetic Energy	Second Order Upwind
Turbulent Dissipation Rate	Second Order Upwind
Energy	Second Order Upwind

Residuals of CFD model

The convergence of continuity, X-Y-Z velocities, energy, and turbulence residuals for both channels are seen in Figure 14. A convergence criteria of 1×10^{-6} was determined to be acceptable for all residuals.

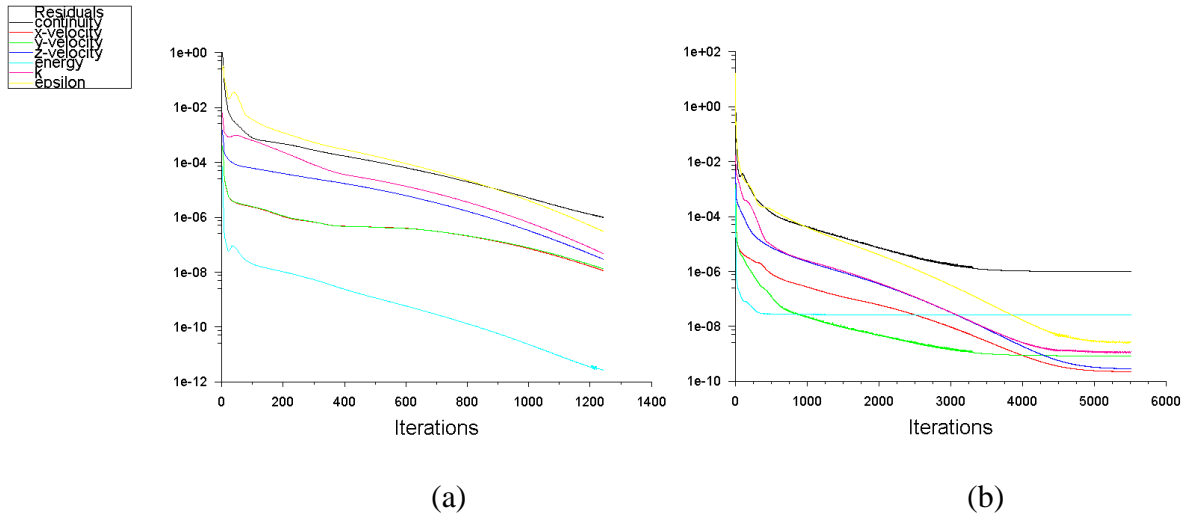


Figure 14: Model residual convergence for (a) 6x6mm circular channel and (b) 20x1.8mm elliptical channel.

Limitations of CFD model

Because the surface roughness characteristics were not fully understood for elliptical sections, no effects due to the roughness of additively manufactured channel walls were modeled. All pipe walls used default ANSYS Fluent roughness properties. Therefore, the influence on turbulent flow and convection cooling due to rough surfaces were not observed through simulation. The material condition was also not considered in the model, so the differences in material properties between various manufacturing methods was not observed through simulation.

Validation of CFD Results

To ensure that the results of the simulation were not significantly affected by mesh quality, the simulation was ran lower mesh resolutions. 5 runs were performed, and the results are listed in

Table 14.

Table 14: Mesh quality of various runs and the resulting CFD outputs.

	Simulation	Run 1 (fine)	Run 2	Run 3	Run 4	Run 5 (rough)	Unit
Nodes	2,370,414	2,133,650	1,769,598	1,538,736	772,001	395,116	n/a
Elements	8,098,772	7,413,300	6,244,852	5,613,828	2,681,955	1,649,437	n/a
Heat Transfer Rate	352.672	352.675	352.677	352.677	352.713	352.066	W
Turbulent Intensity	5.201	5.202	5.205	5.205	5.231	5.332	%
Turbulent Kinetic Energy	0.768	0.768	0.770	0.770	0.778	0.814	m ² /s ²
Velocity Magnitude	13.479	13.479	13.481	13.481	13.507	13.510	m/s
Wall Temperature	569.386	569.379	569.355	569.355	569.104	569.269	C

The results of these simulations was recorded and compared to the results of the final simulation. Figure 15 indicates that as the number of mesh elements increased up to roughly 90% of the final experimental value, the results were no longer changed significantly by mesh quality.

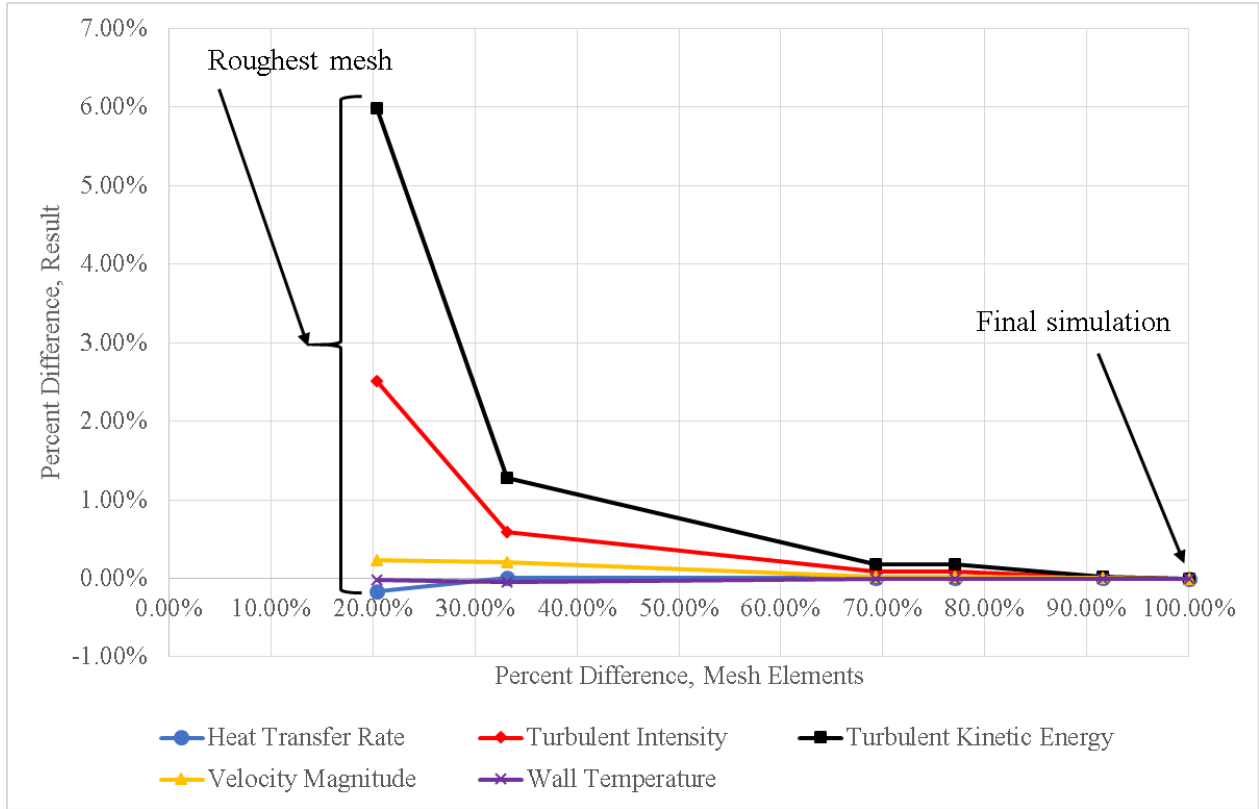


Figure 15: Percent difference in CFD results vs. mesh elements.

CFD Results

The simulation results suggest that despite the lower flow rates measured from experimental results, the elliptical channel had a higher rate of heat transfer than the circular channel. While it seems contradictory that less coolant flow can give a greater rate of heat transfer, the trend can be explained by the increased turbulent intensity of the coolant flow. There is also more surface area on the channel walls for tight elliptical channels where heat transfer can occur.

Simulation results are in

Table 15.

Table 15: Results of simulation.

Output	6x6 circle	20x1.8 ellipse	Unit
Heat Transfer Rate	352.7	550.3	W
Mass Flow Rate	0.380	0.237	kg/s
Outlet Temperature	15.29	15.75	C
Turbulent Intensity	5.20	6.07	%
Turbulent Kinetic Energy	0.768	0.411	m ² /s ²
Velocity Magnitude	13.48	8.39	m/s
Wall Temperature	23.09	23.59	C

Compared to the 6x6mm channel, the 20x1.8mm channel had a greater rate of heat transfer. The lower mass flow rate of the 20x1.8mm elliptical channel indicated that less coolant was being used, despite the greater rate of heat transfer. This resulted in a greater outlet temperature for the elliptical channel. There are two primary causes. Firstly, the elliptical channel had a larger area of contact with the surrounding material. Secondly, the flow of the narrow elliptical channel had greater turbulence, which should be maximized for cooling channels.

Overall, the contour plots show that the 20x1.8mm channel appears to keep the surrounding mold material cooler. Figure 16 and Figure 17 respectively show the thermal contours for the outer boundaries for the 6x6mm simulation and the 20x1.8mm simulation. Because there was no convection between the outer boundaries and the surrounding environment, these contours only show the thermal effects from conduction at the bottom surface, and convection into the cooling

channel. It was observed that overall, the outer boundaries were cooler were cooler on the block with the 20x1.8mm cooling channel.

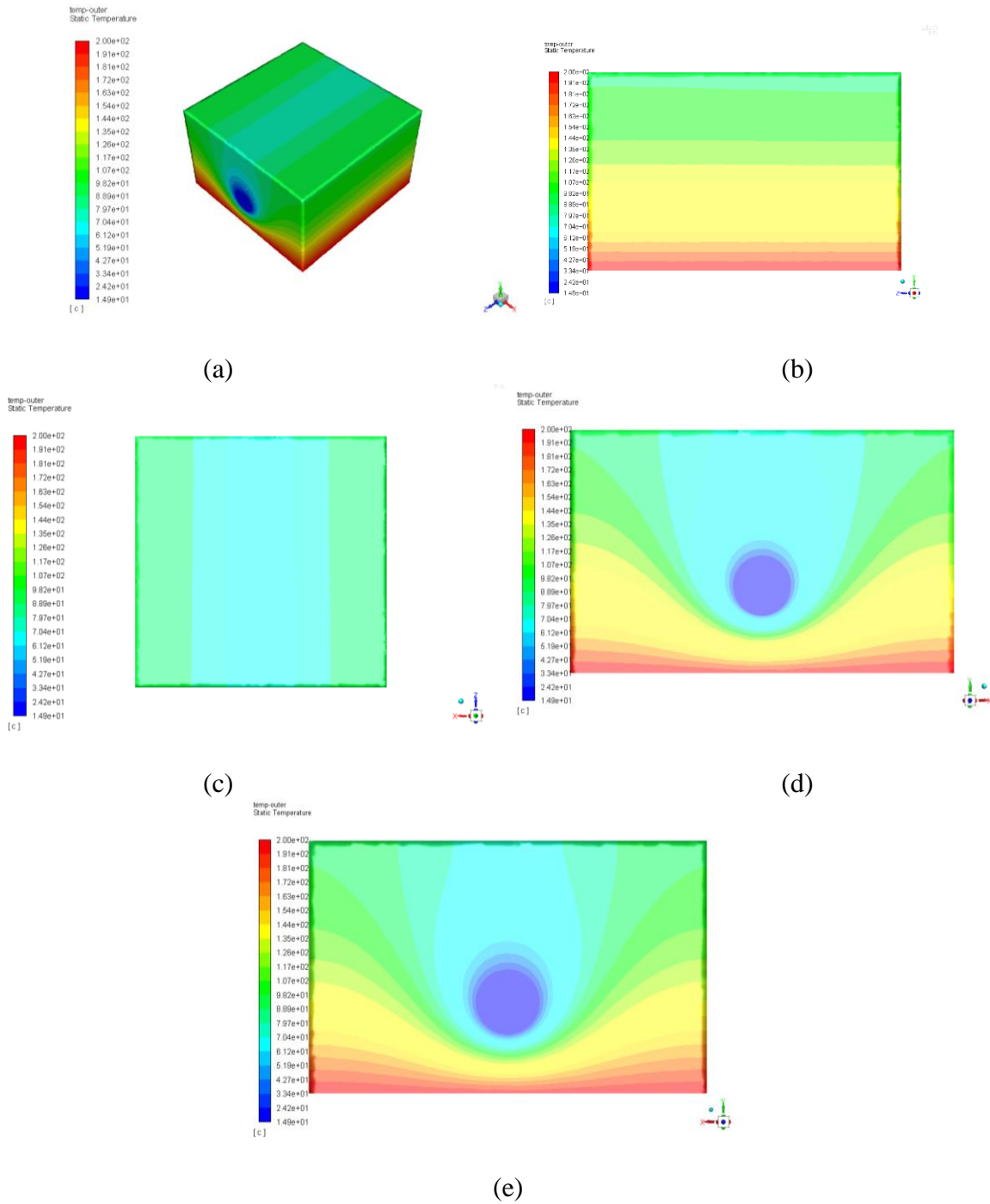


Figure 16: Thermal contours of outer boundaries for 6x6mm simulation.

Views: (a) isometric view, (b) side view, (c) top view, (d) outlet, (e) inlet.

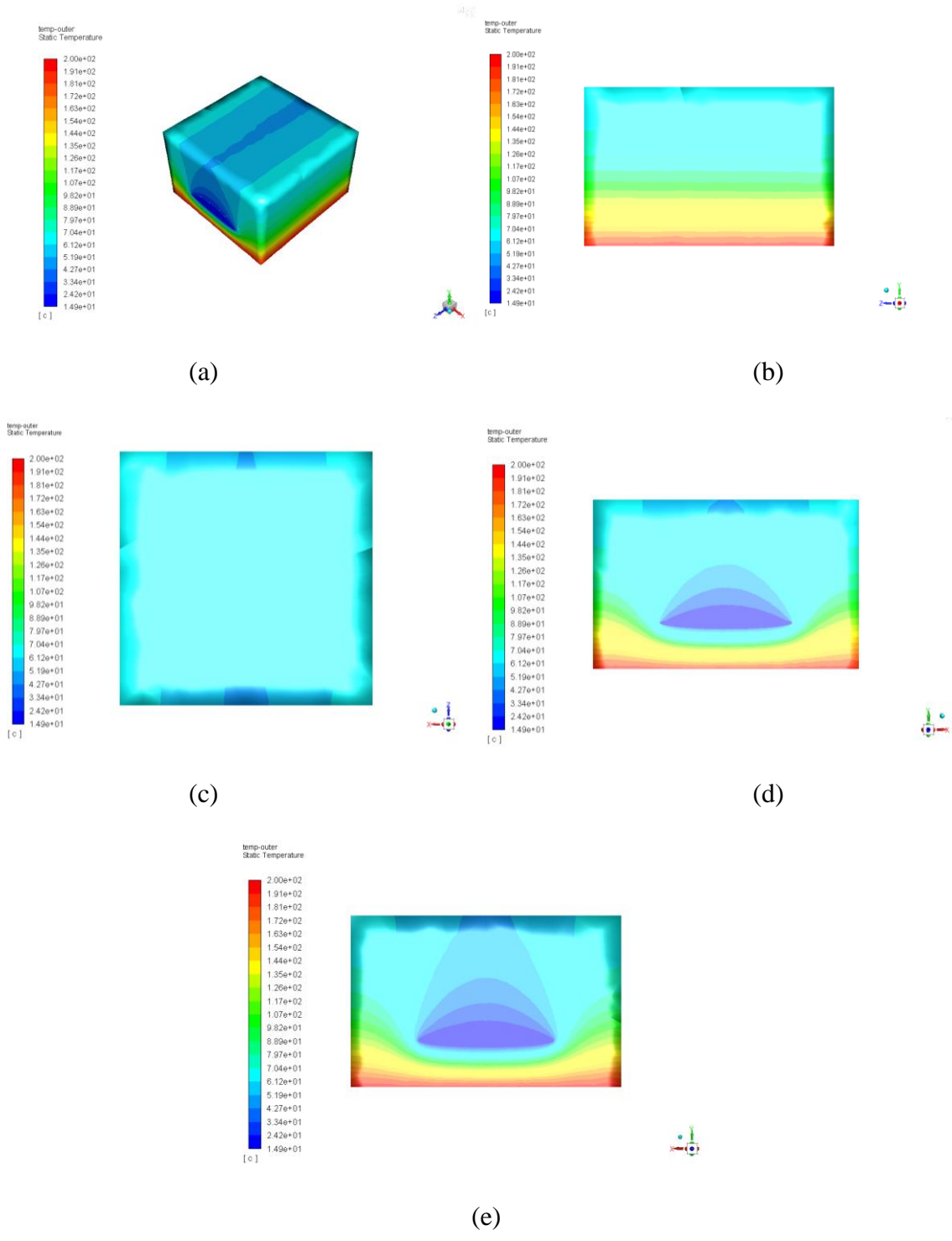


Figure 17: Thermal contours of outer boundaries for 20x1.8mm simulation.

Views: (a) isometric view, (b) side view, (c) top view, (d) outlet, (e) inlet.

Figure 18 and Figure 19 respectively show the thermal contours of mid-channel slices for each simulation. In Figure 19, it is shown that the temperature at the tight corners of the elliptical channel had significant increases in temperature. This was a result of low mean velocity and high turbulence.

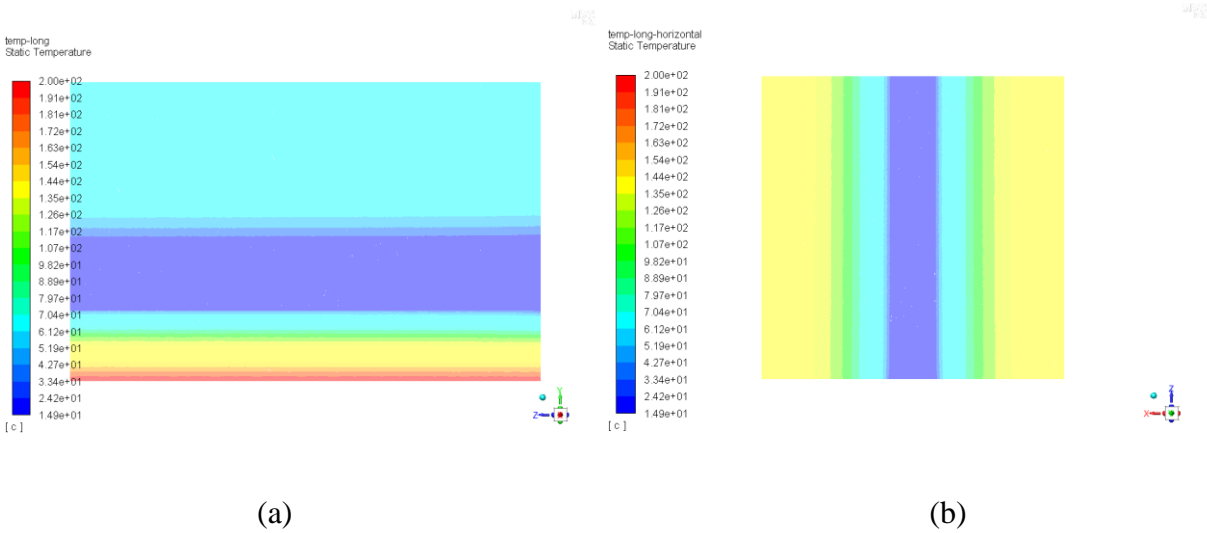


Figure 18: Thermal contours of mid-channel slices for 6x6mm simulation.

Views: (a) side view, (b) top view

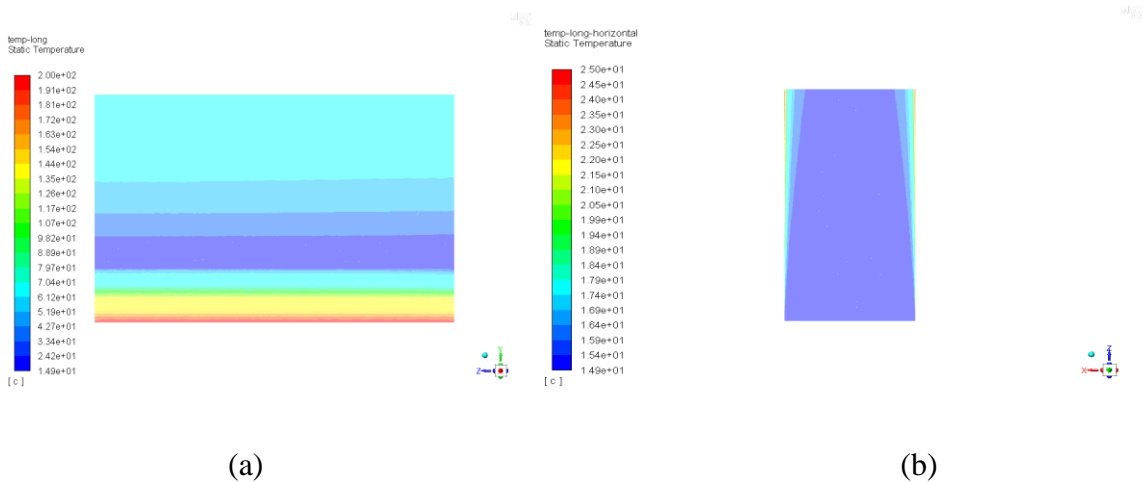


Figure 19: Thermal contours of mid-channel slices for 6x6mm simulation.

Views: (a) side view, (b) top view

Figure 20 and

Figure 21 show the velocity magnitude of each channel at a mid-channel slice. Note that for each figure, the range is from 0.0m/s up to the maximum velocity of the respective channel.

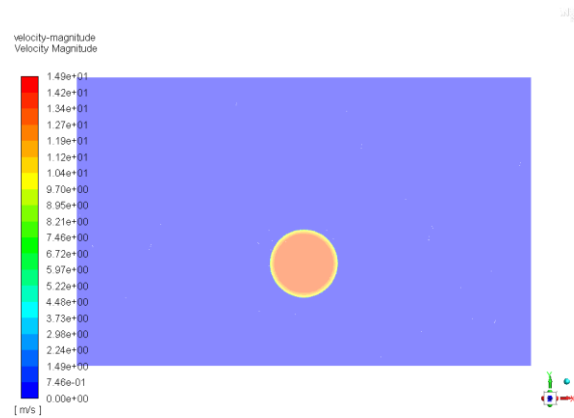


Figure 20: Velocity magnitude contour of front-view mid-channel slice for 20x1.8mm simulation.

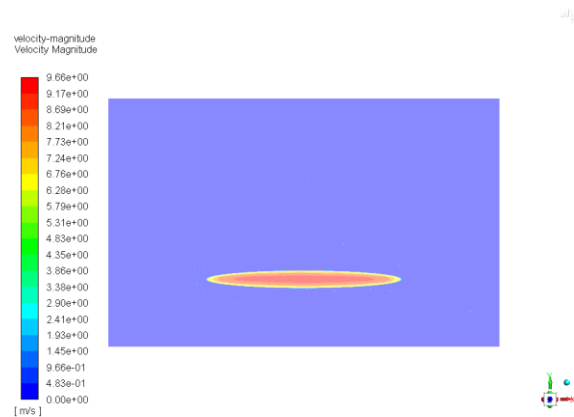


Figure 21: Velocity magnitude countour of front-view mid-channel slice for 20x1.8mm simulation.

One limitation of simulation was that since the material and roughness was not investigated, it cannot be proved that additively manufactured cooling channels have superior cooling properties through this simulated model alone – a physical experiment must be conducted to validate the simulation results.

Creation of Experimental Parts

Fabrication of Machined Cooling Block

The machined block, B1, was fabricated using a 3-axis CNC mill in two lengthwise halves. This was done so the cooling channel would not have to be drilled entirely through the final part. The two halves were pressed together using steel dowel pins. The process plan for fabricating B1 is as follows. The mating surface of each piece was CNC machined using a 0.25” endmill, centerdrill, and drillbit sized for press-fit dowel holes. Machined features include two pockets for tack welds, dowel holes, and a centerhole for the cooling channel. A series of pilot holes was used to make the cooling channel. The final drill size was selected for the reaming process. The inlet and outlet features were CNC machined. The ¼” NPT threaded connections at the inlet and outlet were drilled and tapped. The two pieces were tungsten inert gas (TIG) welded together around the entire perimeter to prevent leakage. The fully assembled cooling channel was finished using a 6mm reamer to ensure that the inconsistencies at the connection were eliminated. The outer surfaces were face-milled. The bottom surface was polished to ensure consistent contact with the heat source.

Build Conditions of Additively Manufactured Parts

In order to ensure the best interior surface finish, the additively manufactured cooling blocks (B2, B3, and B4) were built with the orientation seen in Figure 22. This orientation was

consistent for all SLM-fabricated cooling blocks, including those with circular channels. For complete additively manufactured mold tools, this orientation is also ideal. This is because unlike the cooling channels, the mold cavity can be built with removable supports; in the cavity, the presence of support material is acceptable because it is expected that 3-axis CNC machining will be used as a post-process to create a smooth surface on the cavity. To ensure consistent chamber conditions and build parameters, all additively manufactured parts were produced at once. The build orientation of the surface roughness test pieces (E1, E2, E3, E4) can be seen in Figure 23.

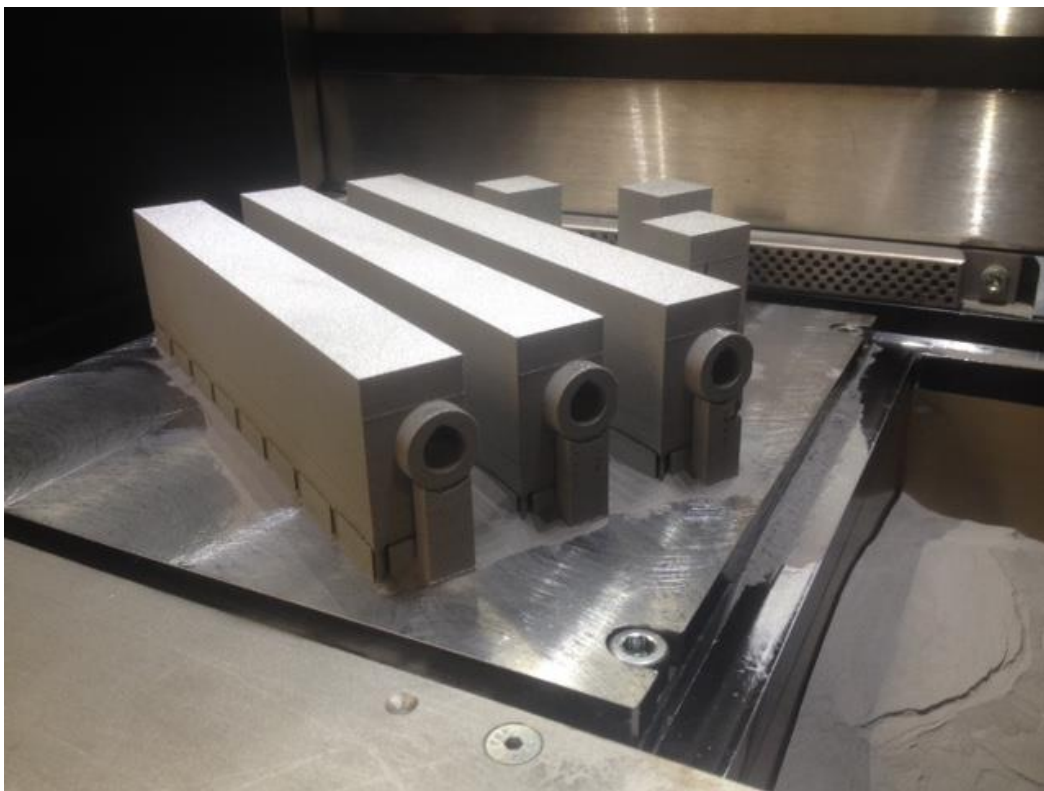


Figure 22: Build orientation of additively manufacturing cooling channels.

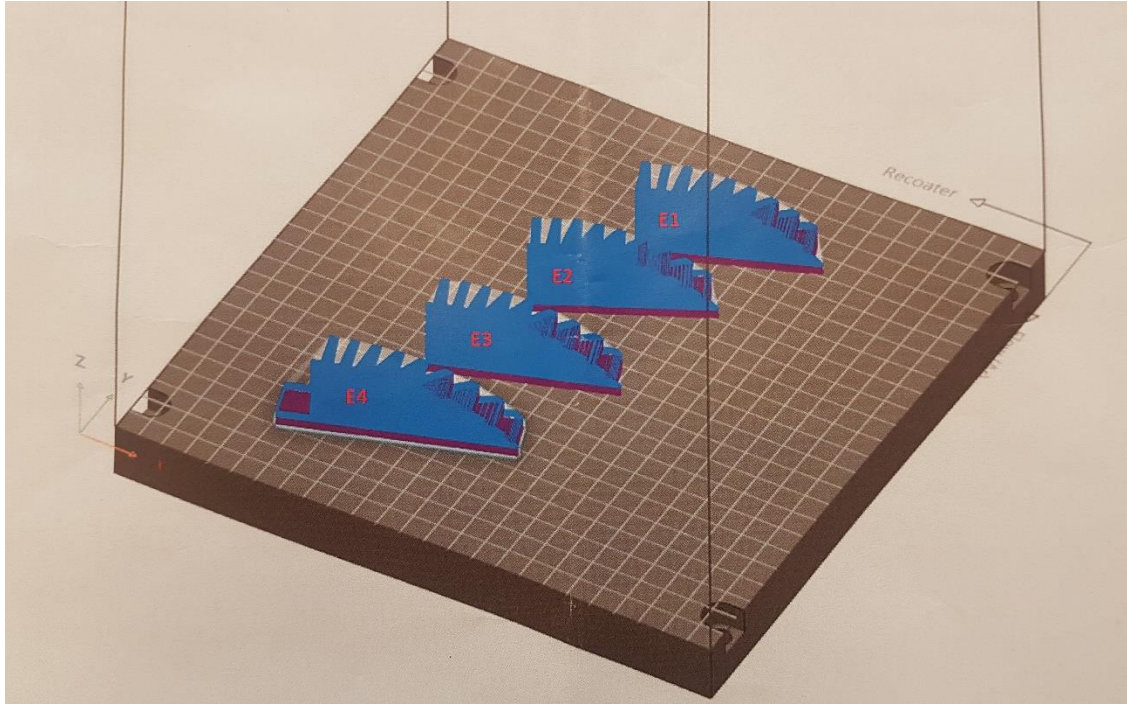


Figure 23: Build orientation of surface roughness test pieces: E1, E2, E3, and E4.

Figure 24 shows how the solid body of the initial parts separated from the raft. To alleviate this issue of delamination, thermal fins were added to the part that acted as cooling fins to allow heat to dissipate more easily from the parts. These fins can be seen in Figure 25. These thermal supports were removed through machining post-print.

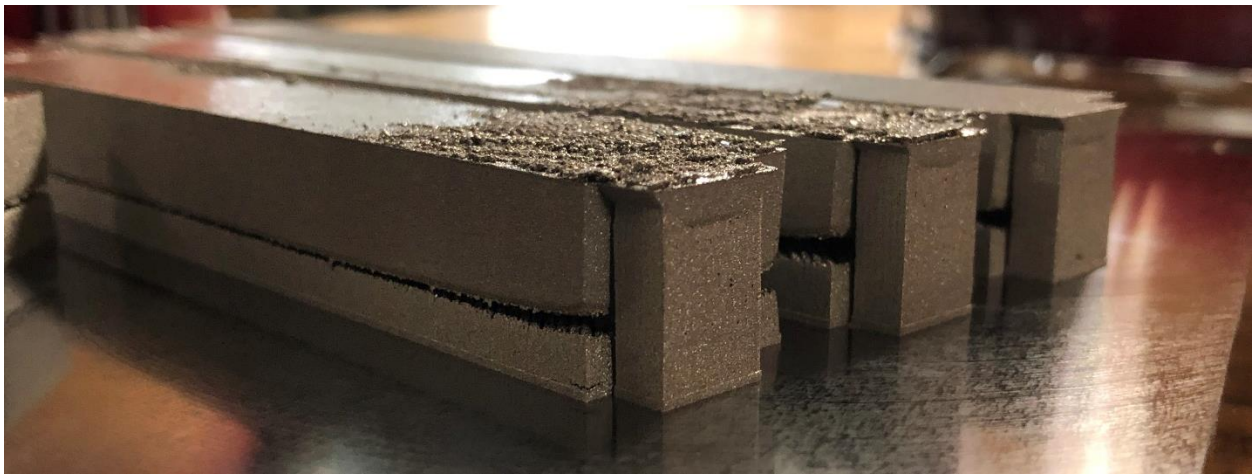


Figure 24: Delamination of failed parts from the raft due to thermal stress.

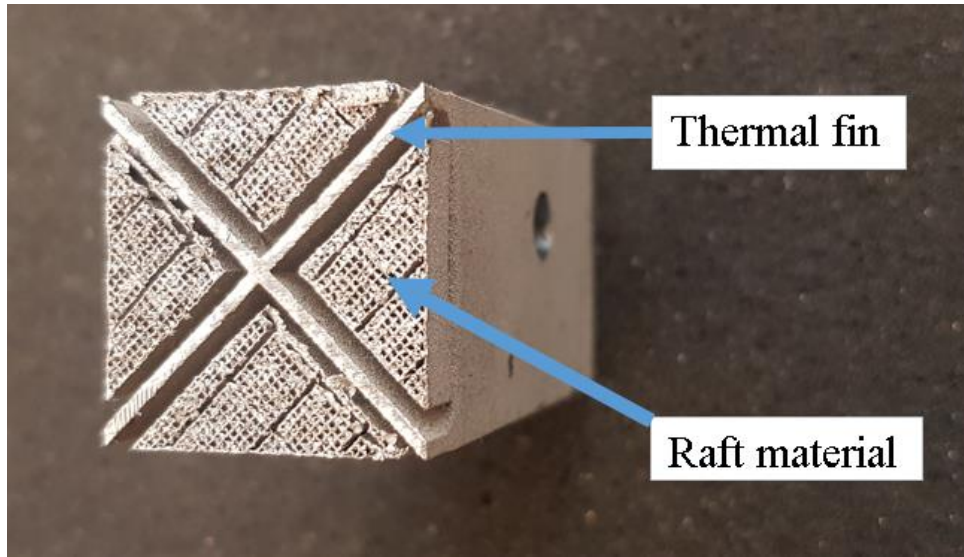


Figure 25: Thermal fin and raft pattern on successfully fabricated parts.

Table 16 shows the material, process, and dimensional differences used for all experimental cooling blocks, B1 through B4, and their sample pieces, C1 through C4.

Table 16: Experimental cooling blocks.

Parts	Primary process	Condition	Wall Roughness	Geometry
B1, C1	Machining	Cast bar, annealed	Machined	6mm circular
B2, C2	SLM	Powdered metal	Machined	6mm circular
B3, C3	SLM	Powdered metal	SLM fabricated	6mm circular
B4, C4	SLM	Powdered metal	SLM fabricated	20mmx1.8mm ellipse

All recorded machine conditions for the successful build are found in Table 17. Laser parameters, which vary based on local part geometry, are seen in

Geometry	Laser Speed (mm/s)	Laser Power (W)	Hatch Distance (mm)
----------	--------------------	-----------------	---------------------

Hatch	Infill	1083	195	0.009
	Upskin	800	135	0.09
	Downskin	1000	80	0.1
Contour	Standard	800	110	
	Down	2000	0	
	On Part	630	110	
Edge	800	60		

Table 18. These values were given by the operator of the EOS M 290 machine that was used.

Table 17: Machine conditions for EOS M 290.

Material	316L Stainless Steel
Powder Part Number	9011-0032
Layer Thickness	0.020 mm
Powder Size (Maximum Particle Size)	$\geq 53 \mu\text{m}$
Beam Offset	0.05 mm for 0.020 mm layer
Build Plate Temperature	80 °C

Geometry	Laser Speed (mm/s)	Laser Power (W)	Hatch Distance (mm)	
Hatch	Infill	1083	195	0.009
	Upskin	800	135	0.09

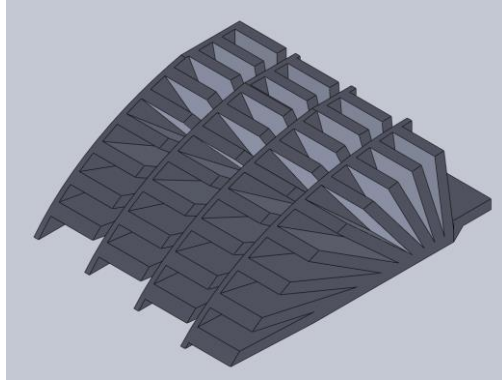
	Downskin	1000	80	0.1
Contour	Standard	800	110	
	Down	2000	0	
	On Part	630	110	
Edge	800	60		

Table 18: Laser speed, power, and hatch distance for various geometries.

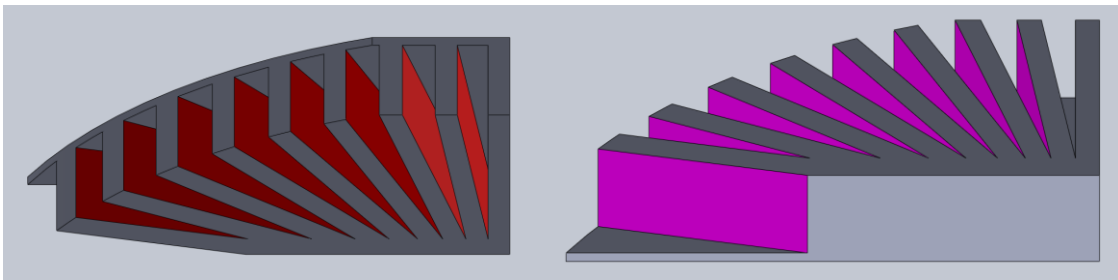
Calculation of Supported Surface Roughness

Unlike machined channels, where the surface roughness of the wall is largely consistent, the roughness of a SLM-manufactured channel wall varies as a function of the build angle. This poses a challenge in the application of the conventional model of pipe friction factors given surface roughness. Additionally, local flow characteristics will be most affected by the surface roughness of the closest wall regions.

In order to determine how the surface roughness changes as a function of build angle, the parts in Figure 26 were additively manufactured using the SLM process with 316L stainless steel. The tabs of various angled surfaces were separated, and the surface roughness measurements were taken for both sides to obtain measurements for positive and negative build angles. The roughness measurements were taken with a HOMMEL Tester 500 surface roughness profilometer.



(a)



(b)

(c)

Figure 26: CAD model of build-angle to surface roughness test parts. (a) isometric view of E1, E2, E3, and E4 (b) (c) cross sections of E1 showing positive (red) and negative (purple) build surfaces

In order to determine surface roughness using experimental materials, process conditions, and build orientations, four test parts were created: E1, E2, E3, and E4. This was done in four parts to distribute heat into four separate smaller bodies. Unfortunately, large surfaces for the negative build angles were not printed without supports. So, the surface roughness of unsupported surfaces was not measured.

Surface roughness was measured from -50° to 90° at various points in order to create equations to estimate surface roughness for the supported channel wall at various build angles.

Surface Roughness Measurements of Various Build Angles

The build supports of the surface roughness test pieces were removed, and each angled surface region was separated so measurements could be taken on a flat table. Surface roughness measurements were taken with a HOMMEL Tester 500 surface roughness tester, which was calibrated using a Mahr calibration sample. The average roughness of the $3.07 \pm 0.05 \mu\text{m}$ sample was measured to be 3.02, which was considered to be acceptable. Roughness was measured parallel and perpendicular to the incline of each surface separately. For each direction, 4 measurements were taken and averaged. This setup is shown in Figure 27.

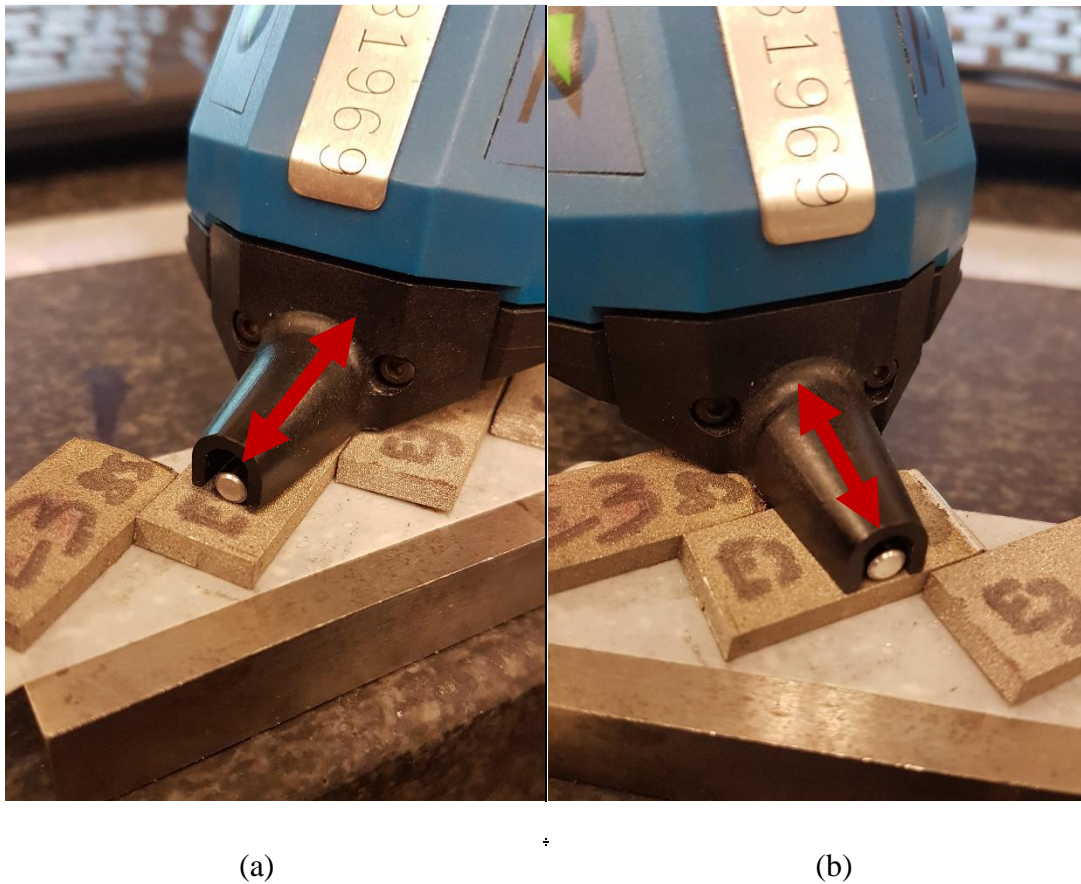


Figure 27: Measurement of surface roughness setup (a) parallel to the direction of incline and (b) perpendicular to the direction of incline.

Each measurement contained two types of surface roughness data. R_a is the arithmetical mean roughness value. This value is obtained by the absolute values of profile height deviations from the mean surface profile. R_z is the mean roughness depth. Specifically, this is the mean value of maximum profile height deviation from the mean surface profile, averaged over a length of 5 segments. This value was obtained using the R_z ISO ten point height method (ISO/DIS 4287/1).

Overall, the averaged R_a values measured were found to be within the specified $13 \pm 5 \mu\text{m}$ range specified by the material manufacturer [1]. The averaged R_z values were found to be within or below the specified $80 \pm 20 \mu\text{m}$ range. The R_a data and trend lines can be seen in Figure 28, and the R_z data and trend lines can be seen in Figure 29.

shows the equations and fit for the second-order polynomial trendlines. These results indicate that for both R_a and R_z , the smoothest surfaces are fabricated at 0 degree vertical or 90 degree horizontal build angles.

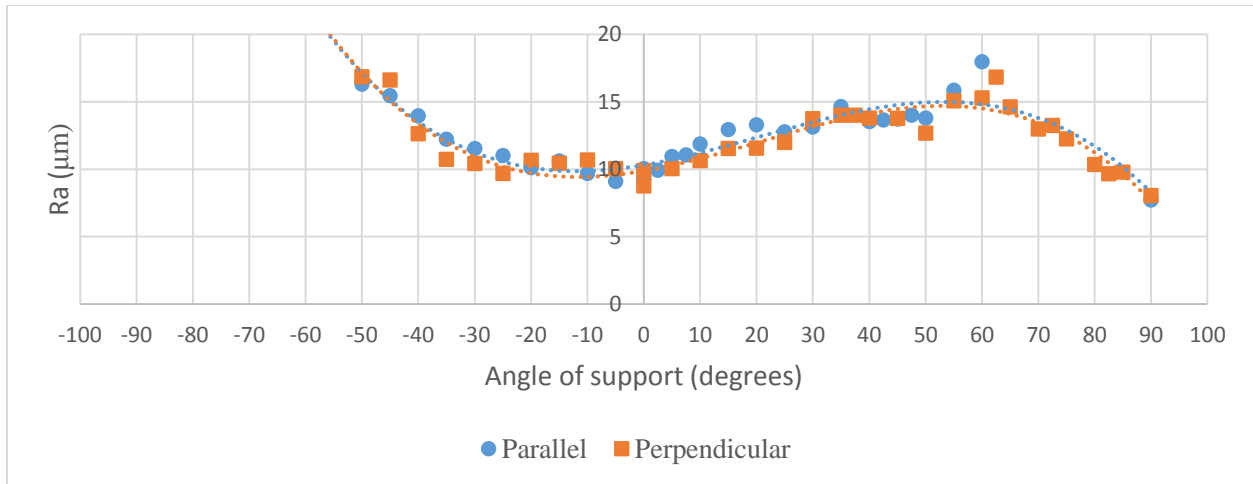


Figure 28: R_a data for various supported angles.

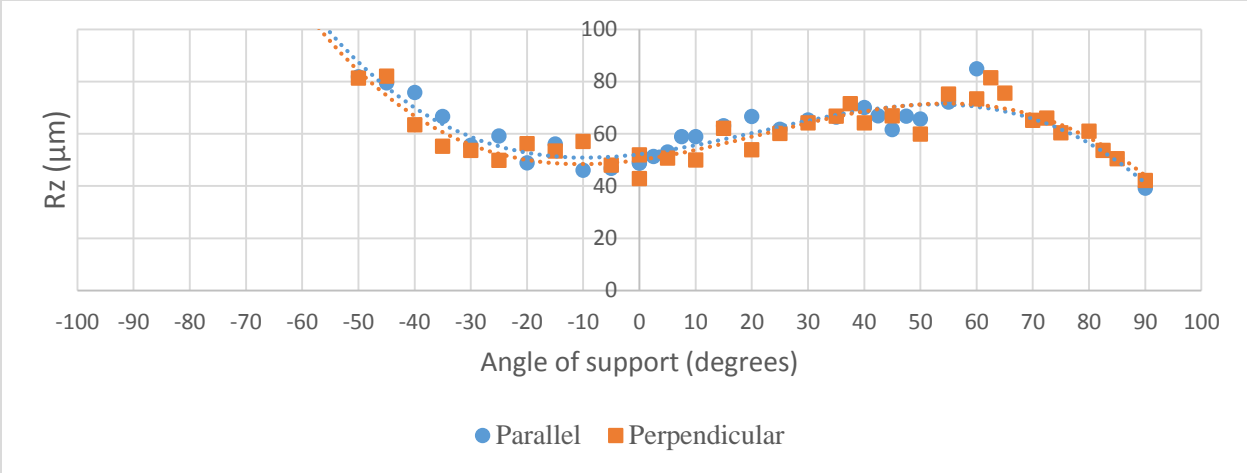


Figure 29: Rz data for various supported angles.

Table 19: Equations and R² values for 2nd order polynomial models.

Surface Roughness	Equation	R ²
Ra - parallel	= -4E-05x ³ + 0.0023x ² + 0.0707x + 10.311	0.8564
Ra - perpendicular	= -4E-05x ³ + 0.0024x ² + 0.0719x + 9.8717	0.8656
Rz - parallel	= -0.0002x ³ + 0.0108x ² + 0.2537x + 52.174	0.8148
Rz - perpendicular	= -0.0002x ³ + 0.0111x ² + 0.2885x + 50.015	0.7999

Approximating Average Roughness of Cooling Channel

The equations found in the previous section were used to approximate the average roughness across the entire supported section of the channel wall. Note that the angular scale for supported surfaces has been shifted in Equation 16 from -60 to 90 degrees to 0 to 150 degrees so that the angles can be correctly used in the arctangent trigonometric function. This is the only calculation where this different angular scale is used. A detailed formulation of this average surface roughness calculation can be seen in the appendix. For the supported region of the channel wall, the average roughness R_{avg} (μm) of a cooling channel wall will be defined in Equation 16 as:

$$R_{avg} = \sum_{i=0}^{n(0 \text{ to } 150 \text{ deg range})} \frac{R_i L_i}{P_{supported}} \quad \text{Equation 16}$$

where R_i is the theoretical R_a or R_z value for the midpoint of segment I of the wall in μm , L_i is the length of segment I in mm, and P is the perimeter of the supported region of the channel in mm.

Table 20 compares various ellipses to a circular cross-section by percent reduction in three categories: unsupported area percentage, R_a of supported area, and R_z of supported area. The results in

Table 20 indicate that there is a small reduction in surface roughness for ellipses as the build height-to-width ratio increases. The equations for perpendicular R_a and R_z measurements were used, to match the direction of coolant flow through the channel.

Table 20: Comparison of theoretical average R_a and R_z values for the supported wall of various elliptical cross sections.

Build height	6	7	8	9	10	12	14	16	18	20	mm
Build width	6.0	5.143	4.5	4	3.6	3	2.571	2.25	2	1.8	mm
% unsupported by EOS design guide	16.7%	12.8%	10.0%	8.0%	6.5%	4.6%	3.4%	2.6%	2.0%	1.7%	
% reduction from circle	0%	23%	40%	52%	61%	73%	80%	85%	88%	90%	
R_a of supported area	12.5	12.2	12.0	11.7	11.5	11.1	10.8	10.6	10.5	10.4	μm
% reduction from circle	0%	2%	4%	6%	8%	11%	13%	15%	16%	17%	
R_z of supported area	60.1	59.5	58.6	57.6	56.7	55.2	54.1	53.3	52.7	52.2	μm
% reduction from circle	0%	1%	3%	4%	6%	8%	10%	11%	12%	13%	

Verification of Roughness Analysis

Roughness Testing of Sample Channels

To determine if the roughness model accurately predicted the surface roughness of various regions of the channel wall, the same test procedure and apparatus were used to investigate the roughness of the channel of the sample pieces. Roughness measurements were taken along the inner channel of blocks C1, C2, and C3, which were fabricated to be cross-sectional samples of B1, B2, and B3. C4, the 20x1.8mm elliptical cooling channel sample, could not be tested because the roughness testing probe would not fit into the channel to obtain measurements. Sample piece

C1 had a reamed channel surface inside a cast, annealed piece of stock 316L stainless steel. Sample piece C2 had a reamed channel surface inside an additively manufactured piece of 316L stainless steel. Sample piece C3 had an as-fabricated surface inside an additively manufactured piece of 316L stainless steel. It was expected that C1 and C2 would have fairly consistent surface finish across the entire channel surface from the reaming operation. The channel walls of C3 were predicted to vary in roughness as a function of the angle of support with the relationship observed in 0. For C1, C2, and C3, the R_a value is seen in Figure 30, and the R_z value is seen in Figure 31. Since C1 and C2 are reamed and do not truly have an “angle of support” along the channel walls, the angle of support simply refers to the orientation at which the measurements were taken for these samples. Sample C4, which had an 1.8x20mm elliptical channel with an as-fabricated surface, was created as well; however, due to the narrow width of the channel, a surface profilometer could not be used to analyze this sample quantitatively.

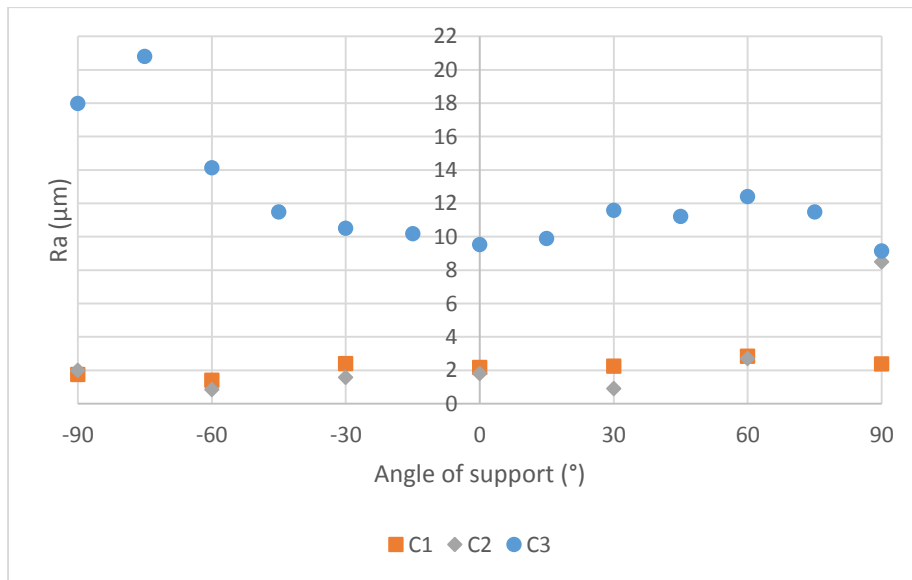


Figure 30: R_a surface roughness at various angles for C1, C2, and C3.

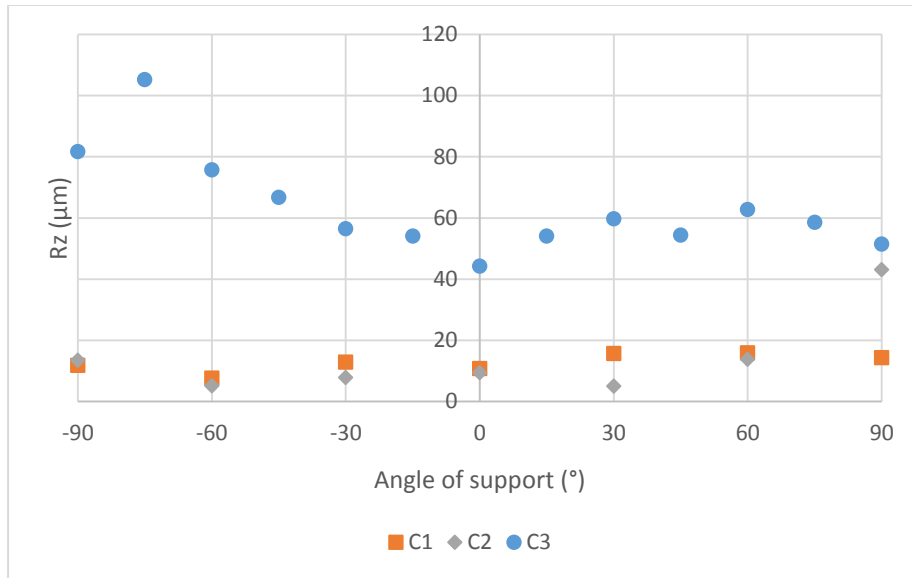


Figure 31: R_z surface roughness at various angles for C1, C2, and C3.

In Figure 32 and Figure 33, R_a and R_z values are respectively compared between the C3 channel and the surface roughness model. It can be seen that for the range of angles where the build can be supported (-60 to 90 degrees) that the model fits the true measurements to some degree of accuracy. The differences between the C3 measurements and the model are seen in Table 21. A significant difference between the model and the raw data is seen at -60° . The model predicts greater roughness than what was measured at significantly negative build angles. For significantly positive build angles, the measured roughness was greater than expected, notably for R_z . Between extreme negative and positive build angles, the measured roughness of C3 appeared to be slightly lower than the theoretical model.

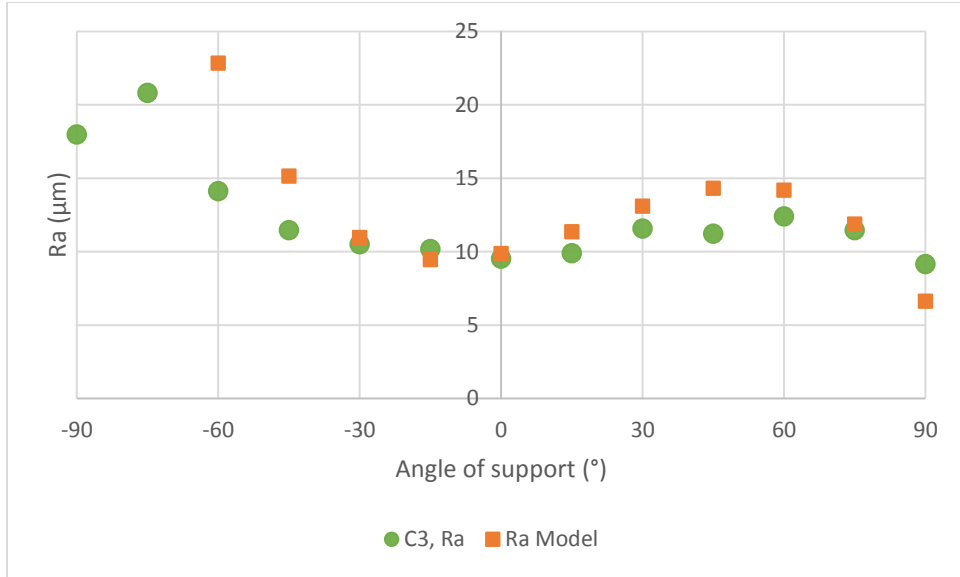


Figure 32: R_a surface roughness of C3 compared to the model.

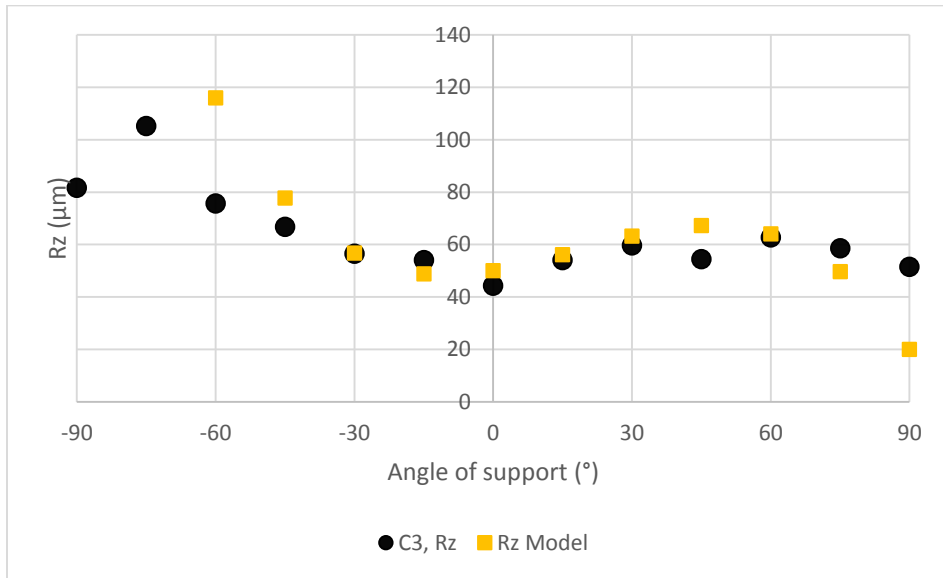


Figure 33: R_z surface roughness of C3 compared to the model.

Table 21: Percent difference between measured surface roughness of C3 and the models for roughness.

C3 Measurement		Model		Angle	% difference	
Ra	Rz	Ra	Rz		Ra	Rz
14.125	75.725	22.8377	115.865	-60	-47%	-42%
11.475	66.775	15.1412	77.735	-45	-28%	-15%
10.5	56.525	10.9547	56.75	-30	-4%	0%
10.175	54.075	9.4682	48.86	-15	7%	10%
9.525	44.3	9.8717	50.015	0	-4%	-12%
9.9	54.075	11.3552	56.165	15	-14%	-4%
11.575	59.75	13.1087	63.26	30	-12%	-6%
11.225	54.425	14.3222	67.25	45	-24%	-21%
12.4	62.725	14.1857	64.085	60	-13%	-2%
11.475	58.55	11.8892	49.715	75	-4%	16%
9.15	51.475	6.6227	20.09	90	32%	88%

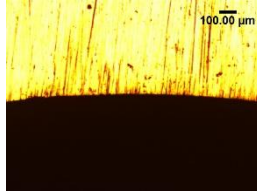
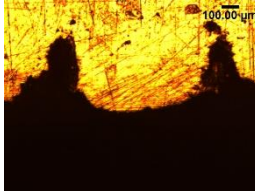
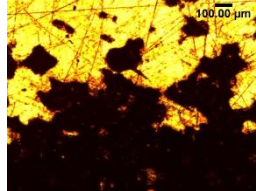
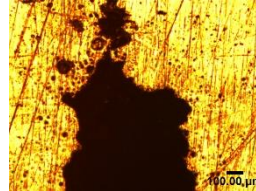
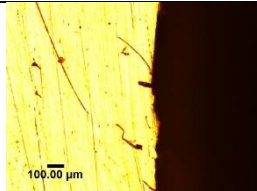
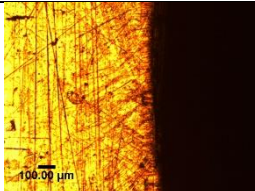
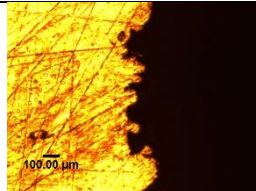
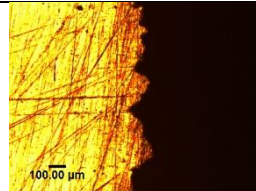
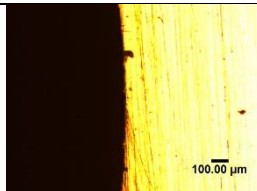
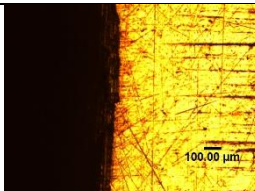
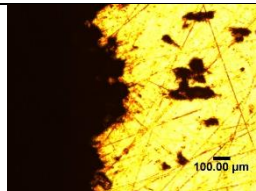
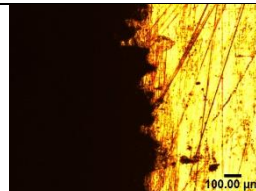
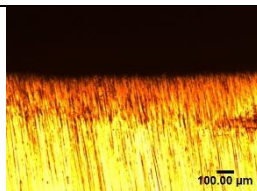
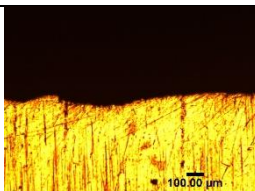
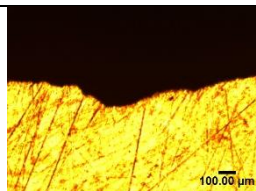
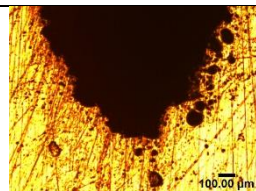
Morphology of Experimental Cooling Channels

The surface morphology of the internal cooling channels was evaluated by inspecting cross-sectional samples using photomicrographs, shown in Table 22. C1 and C2 are the reamed samples from respectively cast and SLM-manufactured material. C3 and C4 are the as-fabricated additively manufactured surfaces for the 6mm circular and 1.8x20mm elliptical channels. The photomicrographs of C1 and C2 demonstrated that reamed channels have less roughness than the as-fabricated surfaces of SLM materials. The tight upper corner of the elliptical channel in sample C4 showed significant build defects as a result of the unsupported fabrication of the material above the channel.

One deviation from the anticipated results was the top region of C2, where the photomicrograph indicated that there was a rough region that did not appear consistent with other reamed surfaces in C1 and C2. Visual inspection of the C2 sample showed that near the top region of the build, there was an area that did not have a machined finish. This is explained by material vacancies at the unsupported top of the channel exceeding the 6mm diameter of the reaming

operation. Before the C2 sample was reamed, the top surface had a roughness value comparable to C3, the sample with a surface finish as-fabricated.

Table 22: Photomicrographs of C1-C4 at four different build regions.

Build Region	C1	C2	C3	C4
Top				
Left				
Right				
Bottom				

Experimental Methodology

In order to compare conventionally machined cooling channels to additively-manufactured conformal cooling channels, four experimental cooling blocks were tested: B1, B2, B3, and B4.

The primary process indicates the method that was used to create the parts from the material of the base condition. For the blocks with machined interior finish, a 6mm reamer was used to obtain a smooth surface. By comparing the flow and cooling properties of each block, the effects of various factors can be compared. Between machined block B1 and B2, the effects due to material differences between cast 316L SS and SLM-processed 316L SS powder can be compared because the cooling channel has identical shape and machined internal features. Between B2 and B3, the flow and cooling properties of the roughness of a machined and additively manufactured channel surface are compared. Between B3 and B4, the difference in cooling channel cross-section can be compared to determine the effects of the major-minor axis ratio for elliptical cross-sections. In this study, two samples were created.

Figure 34 shows the experimental diagram, and the placement various measurements. Pictures of the experimental setup are seen in Figure 35.

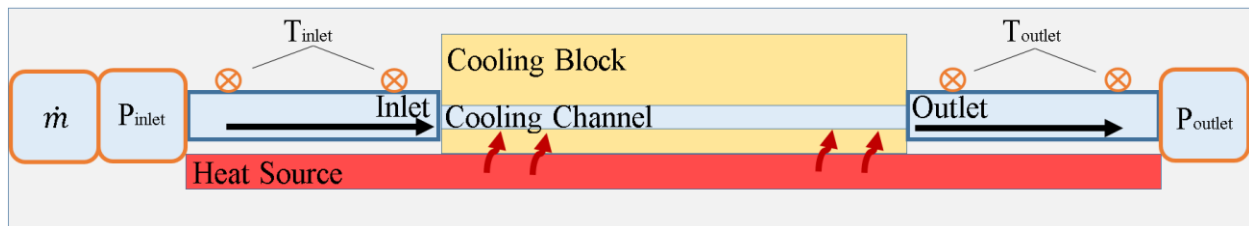


Figure 34: Experimental diagram and the placement of various measurements.

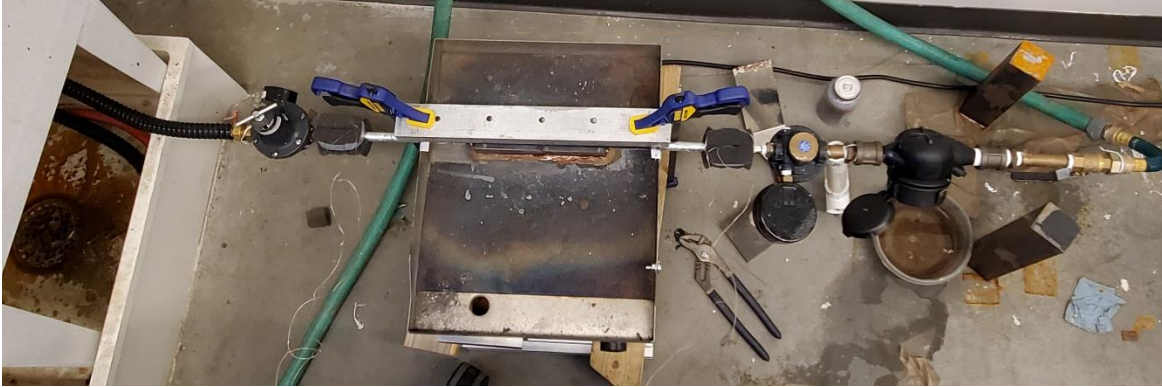


Figure 35: Experimental setup.

Table 23 shows the experimental apparatus that were used. The flow meter that was used was a flow totalizer that recorded the initial and final water volume that entered the system for

each experimental run. The difference was taken for total water flow, and the flow rate was considered the total flow divided by run time, which was taken using a timer.

Table 23: Experimental Apparatus

Function	Product	Notes
Heat source	Yescom Commercial Electric Griddle, SKU YES4367	
Thermocouples: Tinlet, Toutlet	OMEGA type K Adhesive thermocouple	SA1-K-SC
Flow meter	Assured Automation 1/2" home water meter	Mechanical readings
Thermocouple amplifier	Octo MAX31855 5V thermocouple breakout board	
Thermocouple data measurement	Arduino Uno Microcontroller	Code seen in Section 0, Appendix C – Arduino code for thermocouple measurements.

For the heat source, a commercial electric griddle was used in order to achieve a flat surface with a consistent temperature for heat conduction. Temperature controls on the griddle maintain the experimental temperature. The temperature of the water at the inlet and outlet are approximated with two adhesive thermocouples each. In actuality, the thermocouples measure the surface

temperature of the thermally-conductive brass inlet and outlet pipes. For the purposes of this experiment, the temperature at these locations were assumed to be equivalent to the water temperature at a steady state. To further increase precise measurement of the inlet and outlet temperatures, reflective tape was wrapped around the inlet and outlet pipes to insulate the thermocouples from convective heat transfer through the warm air near the heat source. Over the tape covering the thermocouples, the inlet and outlet pipes were also insulated with foam. Additionally, pressure control valves were used to maintain a fixed gauge pressure at the inlet and outlet. Mass flow of the coolant was calculated by using a water flow totalizer; the mass flow rate is calculated as the total amount of water divided by the total experimental time. Each test run was 10 minutes, so the flow rate of a run is calculated as the total flow of water divided by 600 seconds. Thermally conductive Loctite Anti-seize Lubricant was applied between the cooling block and the heat source. This was done to ensure consistency of conductive heat transfer from the heat source into the cooling block. A clamping mechanism was used to apply point forces to push the cooling block onto the heat source to ensure contact. The conduction of heat from the cooling block into this mechanism was minimized by using pointed pins to minimize the area through which heat could conduct.

The effects of convective heat transfer to the air and the surrounding environment were ignored. However, the true walls of convective heat transfer are dimensionally consistent between all cooling blocks. Therefore, the effects due to convection to air were assumed to be comparable for all cooling blocks.

Experimental Parameters

The experimental parameters and values are seen in Table 24. If a value is listed in addition to the unit, the experimental parameter is fixed.

Table 24: Experimental values.

Experimental Parameter	Value or unit	Notes
Heat source temperature	200 °C	Set as maximum griddle temperature. Range determined through observation with an infrared camera
Inlet gauge pressure	25±1.5 lb/in ²	Pressure fluctuated between 23.5 and 26.5 lb/in ²
Outlet gauge pressure	0 lb/in ²	No increase or decrease observed.
Experimental time	600 seconds	t
Coolant/water volumetric density	3.785411 kg/gal	ρ_v
Specific heat of water	4186 J/kg°C	c
Inlet temperature	°C	T_{inlet}
Outlet temperature	°C	T_{outlet}
Total mass flow	gal	V
Temperature difference	°C	$T_{inlet} - T_{outlet}$
Mass flow rate	kg/s	$\dot{m} = \frac{V\rho_v}{t}$
Rate of heat transfer	W	$\dot{Q} = c\dot{m}(T_{out} - T_{in})$

The heat source temperature was set to 200 °C. This was done in order to maximize the rate of heat transfer for ease of observation and to make comparisons between different setups easier to compare.

Calibration of Thermocouples

The experimental cooling circuit was allowed to flow without a source of heat and to normalize all thermocouple readings. This was based on the assumption that as long as the heat source is not powered, passive increase or decrease in water temperature was negligible across the inlet and outlet thermocouple regions. Additionally, it was assumed that since the aluminum block was at thermal equilibrium, the three thermocouples measuring surface temperature should be fairly uniform. Calibration was performed before each day of experimental runs to ensure close accuracy. This was done after the experiment was set up and assembled, but before the heat source was turned on.

References

[1] EOS Stainless Steel 316L Material Datasheet, 2014.

CHAPTER 4. RESULTS AND DISCUSSION

Each experimental run provided an average temperature and flow rate over the run time. These runs were averaged to obtain the experimental rates of heat transfer in Table 25 **Error! Reference source not found.**, and the experimental flow rates of Table 26.

Table 25: Experimental rates of heat transfer.

Test block	Rate of heat transfer, W									
	Mean	Std Dev	Min	Max	1	2	3	4	5	6
B1	1805	252	1404	2073	1404	1707	2073	2053	1718	1879
B2	1070	46	1020	1113	1104	1020	1042	1113		
B3	1095	198	803	1364	1068	1186	803	953	1364	1198
B4	589	100	484	719	484	541	669	532	719	

Table 26: Experimental flow rates.

Test block	Flow rate, kg/s						Raw data flow rate, gal/min			
	Mean	Std Dev	Min	Max	1	2	3	4	5	6
B1	0.381	0.0062	0.374	0.390	6.08	5.93	5.95	6.09	6.19	6.00
B2	0.349	0.0057	0.343	0.354	5.44	5.47	5.61	5.62		
B3	0.325	0.0029	0.321	0.328	5.11	5.09	5.17	5.19	5.19	5.19
B4	0.237	0.0052	0.231	0.241	3.68	3.66	3.83	3.81	3.82	

The B1 block, which was machined from a cast and annealed bar of 316L stainless, was compared to the B2 block, which was SLM-manufactured but used the same finishing methods for the channel wall. The intent was to determine if the powder metal material and the LBPF process had an effect on thermal conductivity compared to traditional cast material. The results indicate that SLM-manufactured and cast/annealed 316L stainless steel materials do not have similar ability to conduct heat for this application. The as-cast, annealed 316L stainless steel exhibited superior cooling performance in this experiment. Historically, porosity of laser powder bed fusion-

processed metals was a significant issue in applications regarding the conduction of heat. It is important to note that the SLM process parameters have an effect on the thermal conductivity of the part. Advancements in the SLM process have greatly reduced the porosity of most metals in recent decades. The B2, B3, and B4 photomicrographs of Table 22 indicate there is the greatest porosity in material subjected to unsupported build conditions. Significant porosity could potentially reduce the ability to conduct heat through the metal, beyond the channel wall. It is important to note that this experiment only compared the material condition of 316L stainless steel. Other metal powders for LPBF processes, notably tool steels used for high-volume-production injection mold tools, cannot be compared against cast material from the results of this experiment.

Comparing the results of the reamed B2 and the B3 block, which was tested as-fabricated with the surface finish obtained from the SLM process, shows that the rate of heat transfer of additively manufactured molds are comparable for channels with reamed surfaces compared to the as-fabricated condition. The coolant flow rate of B2 was greater than B3, which suggests a lower pipe-friction factor due to the lower surface roughness of the reamed surface. This is confirmed by the surface roughness analysis which compared the roughness of reamed versus as-fabricated channels. Despite lower coolant flow rate, the rate of heat transfer is comparable. Considering the relationship between pipe wall roughness and Reynolds number established in Equation 5, where greater wall roughness results in greater turbulence, a higher Reynolds number is expected for B3 compared to B2. This would improve the cooling properties of flow, explaining why the rate of heat transfer is lower even though the flow rate is lower for B3. For injection mold makers, reducing the use of coolant while maintaining the same cooling performance would be considered a benefit.

Comparing the results of B3 and B4 shows that the elliptical cross section did not exhibit superior cooling properties compared to a circular channel of the equivalent cross-sectional area. Although the increase in coolant temperature was comparable, the difference in flow rate between the circular and elliptical channels was significant. This is the greatest factor that reduced the rate of heat transfer in B4. From the elliptical channel of sample C4, the photomicrographs of the top and bottom of the channel indicated that the lack of support for the ellipse was significant. The existence of unmolten or partially molten particles in the tight corners of the 20x1.8mm channel greatly increase the local surface roughness of the channel, which results in reduced flow rate.

In the experiment, the material and flow conditions of machined B1 block were comparable to the simulated CFD model of the 6x6mm circle. The rate of heat transfer per unit length of channel was used to compare results of the simulation and experiment, as the lengths were different. The experimental rate of heat transfer per millimeter of circular channel was 8.82 W/mm in the simulation, and 8.88 W/mm for the B1 block.

Table 27 compares the rates of heat transfer and flow rates from the simulation and experiment. Because the additively manufactured samples do not have the same thermal conductivity and a complex range of surface roughness across the channel wall, results cannot be directly compared between the simulation and B2, B3, and B4. In the simulation, an elliptical channel achieved a greater rate of heat transfer compared to a circular channel. In the experiment, the rate of heat transfer was instead lower.

Table 27: Comparison of results from simulation and experimentation.

	Unit	Simulation		Experiment			
		6x6 circle	20x1.8 ellipse	B1	B2	B3	B4
Rate of heat transfer	W	353	550	1805	1070	1095	589
Length	mm	40		203.2			
Watts per mm	W/mm	8.82	13.76	8.88	5.26	5.39	2.90
Flow rate	kg/s	0.380	0.237	0.381	0.382	0.326	0.240

Overall, the results failed to indicate that additively manufactured cooling channels exhibit superior cooling properties compared to cooling channels created using the conventional injection mold making machining processes. Although the results do not indicate that elliptical channels exhibit greater rates of heat transfer compared to circular channels, it is shown that the circular channel of B3 exhibited greater rate of heat transfer than the elliptical channel of B4. In the experiment, the SLM-manufactured circular channel was measured to have a rate of heat transfer of 1095W, and the elliptical channel was measured to have a lower rate of heat transfer of 589W. This shows that changing the width-to-height ratio of the cooling channel has an effect on the rate of heat transfer, which may still offer some benefits to mold designers. For example, a thinner region of a cavity may be cooled by elliptical channels with lower rates of heat transfer, to ensure consistency of cooling with thicker sections. Varying the width-to-height ratio of cooling channels may also be used to manipulate the stresses due to cooling for molded parts where residual stress is problematic.

CONCLUSIONS AND SUGGESTIONS FOR FUTURE WORK

Conclusions

Experimental models of cooling cells for injection mold cooling were simulated and fabricated. ANSYS simulations indicated that elliptical cooling channels demonstrated greater rates of heat transfer, despite lower coolant flow rates. Physical samples using laser powder bed fusion processes were compared against samples created from machining cast materials, demonstrating that in the cast-annealed condition, 316L stainless steel exhibits a greater rate of heat-transfer for the application. An analysis of roughness for reamed and LPBF-fabricated surfaces was performed to compare the surface roughness of various cooling channels, and surface roughness models were created for additively manufactured surfaces with fully supported build angles. The defects from unsupported material at the top of the cooling channel during the build were significant in this study. The surfaces in the cooling channels of the additively-manufactured samples were rougher as-fabricated, which resulted in greater mixing turbulence despite lower flow rates. It was found that the as-cast 316L stainless steel material had greater thermal conductivity than the SLM-processed material, which resulted in decreased cooling performance in the additively manufactured samples. For the additively manufactured samples, an as-fabricated cooling channel had a similar rate of heat transfer to a reamed channel, but required less coolant for comparable levels of heat transfer. The 20x1.8mm elliptical channel had a lower rate of heat transfer and flow rate compared to the 6mm circular channel in the additively-manufactured samples. This conflicted with the results of the simulation, and the differences are explained by the rough channel walls on the physical samples, which were caused by an inability to support internal features on LPBF-based processes.

Future Work

Between elliptical channels of various length-to-width ratios, the cross-sectional area and pressure drop was chosen as a constant for this thesis. Instead, flow rate may be chosen. For a cooling circuit that flows entirely in series, all cooling channels will have the same flow rate. Thus, choosing a constant flow rate for experimentation may be a better method for analyzing various channels of a single cooling circuit. As lower pipe flow rates result from increased surface roughness, the cross-sectional area of additively manufactured channels would be greater than machined channels in this study. Therefore, holding flow rate as a constant instead of cross-sectional area, additively manufactured molds would perform more closely to conventionally machined molds.

The mechanical properties of various additively manufactured channels was not compared. Mechanical stresses in injection mold tools must be considered to ensure proper tool function over the intended mold lifecycle. It is anticipated that there will be a small reduction in tool durability with elliptical cooling channels that run perpendicularly to the mold. The mechanical properties of machined molds are well understood; largely, the mechanical properties of the material are only affected by post-machining processes such as heat treatments or hardening. The mechanical properties of additively manufactured parts is driven by the structural formation of the parts during the build process. One example is how thermal energy is directed to fuse molten material to adjacent regions and layers. Being able to predict mechanical properties of additively manufactured metals will allow further optimization of conformal cooling channels.

This investigation did not look at vertically versus horizontally built cooling channels. It is expected that vertically built cooling channels will exhibit flow and thermal characteristics of pipes with a uniformly lower surface roughness.

The flow and thermal properties of elliptical cross sections have been compared in this investigation. The results of this can be applied to simulation for mold optimization. Cross section as a variable parameter should allow greater flexibility for the local control of flow and cooling. A potential benefit is that regions of the mold cavity that do not have uniform thickness can use cooling channel cross-sections with lower heat transfer rates to cool thinner sections. This may be used to reduce thermal stress through additional control of cooling characteristics.

A thorough exploration of other cross sections is encouraged. For example, a teardrop cooling channel can be fabricated without unsupported surfaces, as long as the upper surface angle does not exceed what is permissible for a particular material. Matrices have been previously studied, but the cooling performance has not yet been thoroughly compared to alternatives. Slots, like ellipses, also reduce the unsupported regions compared to a circular channel.

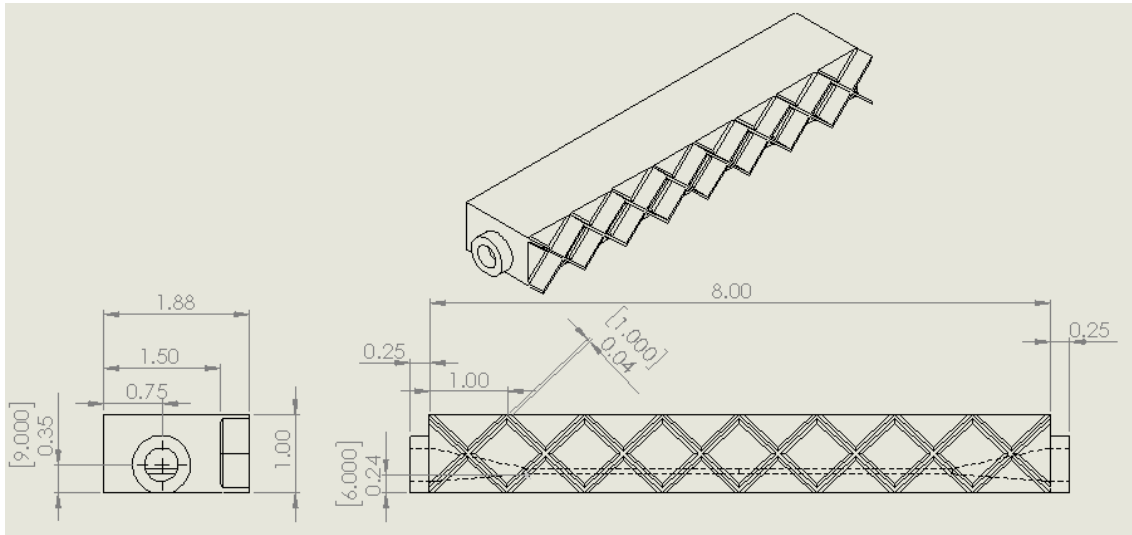
One cross-section that was not examined was a teardrop, with a sharp corner at the top side of the channel during the build. The top side of the teardrop section is angled so that there is adequate supportive material beneath the current build layer. Thus, this channel is fully supported along the entire channel wall. This geometry is easier to additively manufacture than conventional circular channels. A sharp teardrop corner on the top of the channel during the build can likely be combined with elliptical cross-sections to further enhance the overall smoothness of the channel.

This study examined the effects of coolant flow and heat absorption from various cross-sections. The cross-sectional area of the cooling channel can also be examined for coolant flow and heat absorption. For example, using cooling channels with greater cross-sectional area to decrease cooling times on the hotspot of a mold region.

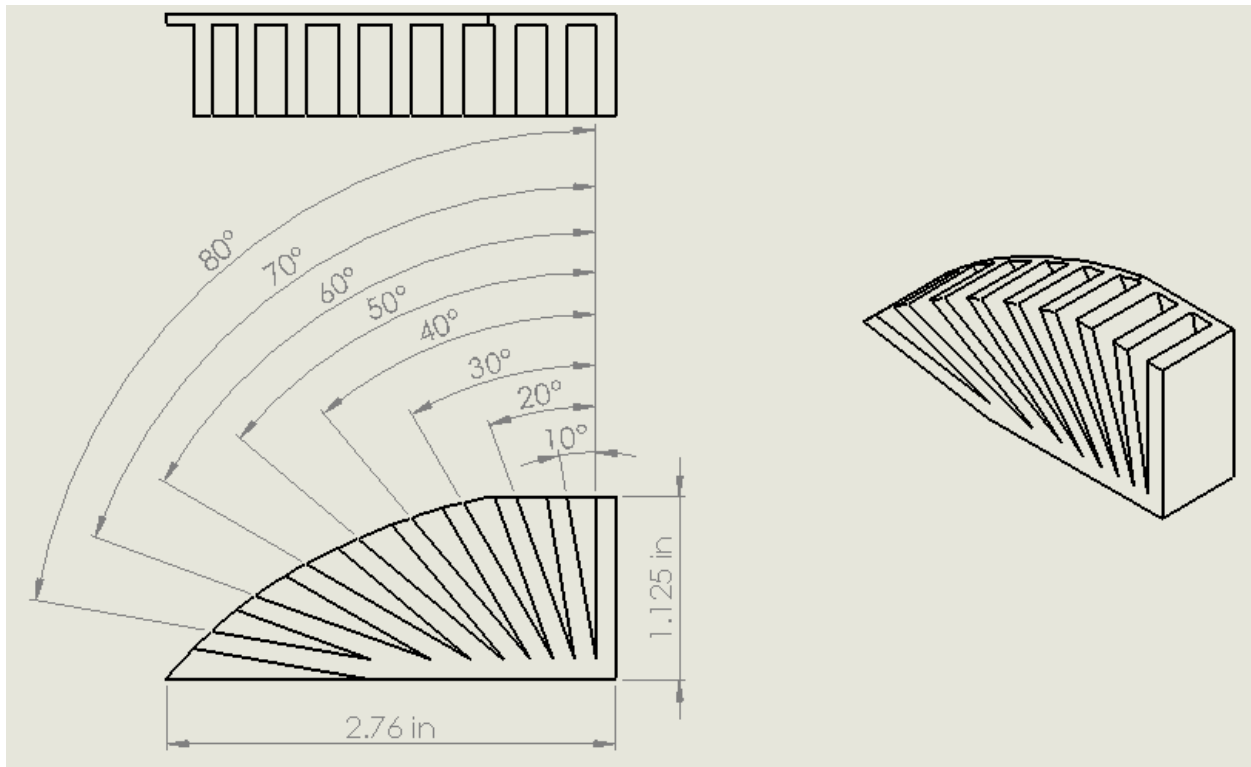
Although the content of this thesis compared the flow and cooling properties of traditionally machined versus additively manufactured molds, transitioning to additively

manufactured molds can be costly for companies. Companies may also hesitate to invest in technologies outside of their core competencies. Most injection molding or tool and die companies are generally proficient at technology and design for mold machining. To increase confidence in additively manufactured molds, factors such as the expected tool life, water consumption, change in cycle time, and fabrication costs should be quantifiable. Then, mold fabrication process decisions can be made based on technical feasibility and economic considerations.

Appendix A – Design of experimental and simulated parts



Reference drawing for B4. All dimensions shown are equivalent between B1, B2, B3, and B4.



Reference drawing for E1. For each angle, the offset for E2, E3, and E4 is $+2.5^\circ$, $+5^\circ$, and $+7.5^\circ$ respectively.

Appendix B – Surface Roughness Data and Example Calculation

Surface roughness data for E1, E2, E3, and E4 measurements.

Angle of support	Block	Roughness (Ra)								Roughness (Rz)								Ra		Rz	
		Parallel to angle				Perpendicular to angle				Parallel to angle				Perpendicular to angle				Parallel	Perpendicular	Parallel	Perpendicular
-50	E1	16.4	16.8	17.8	14.2	17.5	17	14.9	18	78.2	79.8	99.9	69.2	85.5	82.7	70.6	86.8	16.3	16.9	81.8	81.4
-45	E3	14.6	16.3	15	15.9	16.5	17	16	17	72.3	81	70.8	94.1	82.6	79.3	83	83.3	15.5	16.6	79.6	82.1
-40	E1	14.3	12.6	13	15.9	10.6	13.5	13	13.4	72	63.3	72.9	95.2	55.9	64.5	65.6	67.7	14.0	12.6	75.9	63.4
-35	E3	9.9	12.2	14.2	12.6	9.7	11.4	11.5	10.3	50.2	71	77	68.5	54	59.9	57.8	49.3	12.2	10.7	66.7	55.3
-30	E1	11.3	12.2	11.4	11.2	10	10.1	10.2	11.4	56	58.3	54.1	54.2	53	54.2	49.7	56.9	11.5	10.4	55.7	53.6
-25	E3	10.1	11.6	11.5	10.8	10.2	9.8	9.8	8.9	54.6	60.6	69.8	51.5	52.9	50.1	48.8	47.6	11.0	9.7	59.1	49.9
-20	E1	10.2	10.6	9.4	10.2	10.7	11.4	10.7	9.8	47.5	50.4	47.2	50.5	58.8	51.5	59.8	54.8	10.1	10.7	48.9	56.2
-15	E3	10.6	9.9	11.2	10.7	11	9.6	11.5	9.7	55.2	53.7	56.4	59	57.7	49.2	55.8	50.8	10.6	10.5	56.1	53.4
-10	E1	9.6	9.7	9.2	10.2	10.2	11.7	10.1	10.7	48.8	46.8	40.2	48.6	59.1	55.9	56.6	56.5	9.7	10.7	46.1	57.0
-5	E3	10	8	9.5	8.8	8.6	10.5	9.8	11.2	51	45.4	49.3	41.7	42.4	54.2	44	51.5	9.1	10.0	46.9	48.0
0	E1	9.1	7.5	11.7	9	10.2	9.6	10	9.8	51.8	35	60.5	47.5	50.5	51.1	56	50.2	9.3	9.9	48.7	52.0
0	E1	8.6	10.6	10.9	10	8.7	8.3	7.6	10.4	46.9	49	46	54.1	41	37.5	41.1	52	10.0	8.8	49.0	42.9
2.5	E2	11.7	9.9	10.3	7.8					56.6	51.1	53.4	44.2					9.9		51.3	
5	E3	11.6	12.4	9.4	10.4	11.4	8.9	9.1	10.7	52.7	60.6	49.2	49.6	56	45.8	50.5	50.4	11.0	10.0	53.0	50.7
7.5	E4	10.2	10.9	10.5	12.6					48.4	65.2	53.5	68.4					11.1		58.9	
10	E1	11.3	9.9	13.6	12.7	11.8	9.4	10.6	10.7	54.2	51	64.1	66.2	52.5	48	48.8	50.4	11.9	10.6	58.9	49.9
15	E3	12.1	13	13.2	13.4	10.8	11.3	12.9	11.1	58.1	64.5	61	68.9	58.8	66.3	63	60.4	12.9	11.5	63.1	62.1
20	E1	13.6	13.6	11.8	14.2	11	13.1	11.2	10.9	64.9	69.6	57.6	74.7	51.6	57.3	54	52.7	13.3	11.6	66.7	53.9
25	E3	12.1	12	12.1	14.9	10.8	13.4	11.4	12.3	61.2	56.3	60.2	69.5	54.5	64.2	61.4	60.4	12.8	12.0	61.8	60.1
30	E1	13.1	12.4	13.6	13.4	14.5	13.3	12.7	14.5	66.2	63	59.1	73	69.6	62.7	60.8	63.9	13.1	13.8	65.3	64.3
35	E3	12.2	15	14.6	16.8	14.2	13.8	14.8	13.2	56.4	71.5	66.2	71.6	71.5	64.4	71.2	59.8	14.7	14.0	66.4	66.7
37.5	E4					13.1	12.2	15.9	14.8					69	65.3	76.7	75.4		14.0		71.6
40	E1	13.4	12.4	14.2	14.1	13.1	13.5	15.8	12.8	62	73	74.6	70.6	58.3	65.7	69.4	63.5	13.5	13.8	70.1	64.2
42.5	E2	10.9	16.1	14.2	13.4					59.2	72.7	71	64.7					13.7		66.9	
45	E3	13.4	11.2	14.3	16	14.3	12.8	14.2	13.9	65.8	49.1	58.7	72.8	71.2	65.5	65.3	65.4	13.7	13.8	61.6	66.9
47.5	E4	16.5	13.9	12.8	12.8					76.3	65.7	67.8	57.1					14.0		66.7	
50	E1	12.6	14.8	13	14.8	16.2	12.6	10.5	11.4	68	72.9	57.3	64.5	72.4	63.4	50	53.7	13.8	12.7	65.7	59.9
55	E3	14.6	15.4	18.4	15	15.8	16.9	13.2	14.4	65.2	74	78.4	71.2	76.5	79.6	68.6	76.3	15.9	15.1	72.2	75.3
60	E1	18.4	18.3	18.2	17	17.6	15.5	14.6	13.4	87.2	85.7	84.9	82	82.3	70.8	71.2	69	18.0	15.3	85.0	73.3
62.5	E2					20.3	12.6	18.6	15.8					93.9	64.5	86.4	80.9		16.8		81.4
65	E3					11.1	12.8	18.2	16.4					60	76.3	78.4	87.5		14.6		75.6
70	E1					11.4	14.7	14.1	11.7					68.7	64.4	70.2	57.3		13.0		65.2
72.5	E2					14.7	12.1	12.3	13.9					76.7	58	62.4	67.2		13.3		66.1
75	E3					10.9	13.2	13.3	11.6					58.1	57	66.2	60.4		12.3		60.4
80	E1					10.3	11.1	10	10					65	70	58.3	50.8		10.4		61.0
82.5	E2					9.9	9.34	9.1	10.3					59.8	49.92	50.9	53.8		9.7		53.6
85	E3					7.4	7.8	11.6	12.3					37.5	41.8	65.4	57		9.8		50.4
90	E4	8.9	7.3	7.1	7.5	7	8.1	9	8.1	42.5	40.6	39.2	34.4	34.1	39.9	47	47.5	7.7	8.1	39.2	42.1

Surface roughness data for C1, C2, and C3 measurements.

Angle	C1								C2								C3								
	Ra				Rz				Ra				Rz				Ra				Rz				
-90	3.0	2.7	0.4	0.9	17.6	19.6	3.7	6.4	2.4	2.0	1.8	1.8	14.4	10.3	20.0	9.5	12.2	20.6	17.6	21.5	60.7	85.8	83.1	97.1	
-60	1.8	0.1	0.9	2.8	9.9	1.2	5.1	14.3	1.4	0.6	0.5	0.9	7.4	2.9	3.8	6.4	14.2	13.7	13.3	15.3	80.2	83.6	59.4	79.7	
-30	1.4	4.6	2.4	1.2	7.9	24.5	12.6	6.7	1.6	2.6	1.3	0.7	8.9	12.1	6.6	3.8	13.4	9.9	9.0	9.7	70.8	50.8	54.4	50.1	
0	4.3	1.2	1.2	2.0	20.4	6.4	6.1	10.1	1.5	1.7	2.3	1.8	8.1	8.7	11.9	9.0	11.5	8.5	9.6	8.5		41.5	48.6	42.8	
30	1.4	3.2	1.5	2.9	7.6	30.9	9.0	15.4	1.1	0.5	1.2	0.8	5.5	2.8	6.1	6.0	13.1	11.0	11.2	11.0	63.2	55.9	60.0	59.9	
60	1.8	2.4	5.1	2.0	10.3	13.8	28.8	10.7	2.1	2.9	3.6	2.2	9.5	14.9	20.3	10.7	11.2	14.1	12.5	11.8	61.6	67.5	61.2	60.6	
90	2.2	3.9	2.1	1.3	11.6	20.0	11.5	7.4	10.4	5.3	8.1	10.2	52.9	28.0	42.1	49.6	9.2	8.4	9.4	9.6	48.8	45.0	54.6	57.5	
-75																		24.5	14.6	19.9	24.2	130	77.6	97.2	116
-45																		10.4	11.1	9.7	14.7	58.7	63.0	56.0	89.4
-15																		11.5	2.4	10.8	16.0	60.4	25.6	53.1	77.2
15																		6.0	12.3	15.2	6.1	38.1	68.0	78.0	32.2
45																		13.5	11.2	9.6	10.6	58.5	53.2	50.6	55.4
75																		12.7	11.1	12.0	10.1	74.0	49.6	58.1	52.5

Example calculation of average cooling channel wall roughness.

				Build height	6						
				Build width	6.0						
				% unsupported by EOS design guide	16.7%						
				% reduction from circle	0%						
				Ra of supported area	12.5						
				% reduction from circle	0%						
				Rz of supported area	60.1						
				% reduction from circle	0%						
	$R_{avg} = \sum_{i=0}^{n \text{ (to } 150 \text{ deg)}} \frac{R_i L_i}{P}$										
Angle	Radians	Midpoints	Ra	Rz	theta	Midlengths	Li	Li/P	Ra*Li/P	Rz*Li/P	
0	0	-0.02181662	6.6227	20.09	-0.022	0	1.25	0.008333	0.055189	0.167416667	
2.5	0.043633	0.021816616	7.7411	26.25875	0.0218	1.25	2.5	0.016667	0.129018	0.437645833	
5	0.087266	0.065449847	8.7582	31.91	0.0654	3.75	2.5	0.016667	0.14597	0.531833333	
7.5	0.1309	0.109083078	9.6778	37.0625	0.1091	6.25	2.5	0.016667	0.161297	0.617708333	
10	0.174533	0.15271631	10.504	41.735	0.1527	8.75	2.5	0.016667	0.175062	0.695583333	
12.5	0.218166	0.196349541	11.24	45.94625	0.1963	11.25	2.5	0.016667	0.187326	0.765770833	
15	0.261799	0.239982772	11.889	49.715	0.24	13.75	2.5	0.016667	0.198153	0.828583333	
17.5	0.305433	0.283616003	12.456	53.06	0.2836	16.25	2.5	0.016667	0.207605	0.884333333	
20	0.349066	0.327249235	12.945	56	0.3272	18.75	2.5	0.016667	0.215745	0.933333333	
22.5	0.392699	0.370882466	13.358	58.55375	0.3709	21.25	2.5	0.016667	0.222635	0.975895833	
25	0.436332	0.414515697	13.7	60.74	0.4145	23.75	2.5	0.016667	0.228337	1.012333333	
27.5	0.479966	0.458148929	13.975	62.5775	0.4581	26.25	2.5	0.016667	0.232914	1.042958333	
30	0.523599	0.50178216	14.186	64.085	0.5018	28.75	2.5	0.016667	0.236428	1.068083333	
32.5	0.567232	0.545415391	14.337	65.28125	0.5454	31.25	2.5	0.016667	0.238943	1.088020833	
35	0.610865	0.589048623	14.431	66.185	0.589	33.75	2.5	0.016667	0.24052	1.103083333	
37.5	0.654498	0.632681854	14.473	66.815	0.6327	36.25	2.5	0.016667	0.241222	1.113583333	
40	0.698132	0.676315085	14.467	67.19	0.6763	38.75	2.5	0.016667	0.241112	1.119833333	
42.5	0.741765	0.719948316	14.415	67.32875	0.7199	41.25	2.5	0.016667	0.240251	1.122145833	
45	0.785398	0.763581548	14.322	67.25	0.7636	43.75	2.5	0.016667	0.238703	1.120833333	
47.5	0.829031	0.807214779	14.192	66.9725	0.8072	46.25	2.5	0.016667	0.23653	1.116208333	
50	0.872665	0.85084801	14.028	66.515	0.8508	48.75	2.5	0.016667	0.233795	1.108583333	
52.5	0.916298	0.894481242	13.834	65.89625	0.8945	51.25	2.5	0.016667	0.23056	1.098270833	
55	0.959931	0.938114473	13.613	65.135	0.9381	53.75	2.5	0.016667	0.226887	1.085583333	
57.5	1.003564	0.981747704	13.37	64.25	0.9817	56.25	2.5	0.016667	0.222839	1.070833333	
60	1.047198	1.025380936	13.109	63.26	1.0254	58.75	2.5	0.016667	0.218478	1.054333333	
62.5	1.090831	1.069014167	12.832	62.18375	1.069	61.25	2.5	0.016667	0.213868	1.036395833	
65	1.134464	1.112647398	12.544	61.04	1.1126	63.75	2.5	0.016667	0.20907	1.017333333	
67.5	1.178097	1.156280629	12.249	59.8475	1.1563	66.25	2.5	0.016667	0.204147	0.997458333	
70	1.22173	1.199913861	11.95	58.625	1.1999	68.75	2.5	0.016667	0.199162	0.977083333	
72.5	1.265364	1.243547092	11.651	57.39125	1.2435	71.25	2.5	0.016667	0.194176	0.956520833	
75	1.308997	1.287180323	11.355	56.165	1.2872	73.75	2.5	0.016667	0.189253	0.936083333	
77.5	1.35263	1.330813555	11.067	54.965	1.3308	76.25	2.5	0.016667	0.184455	0.916083333	
80	1.396263	1.374446786	10.791	53.81	1.3744	78.75	2.5	0.016667	0.179845	0.896833333	
82.5	1.439897	1.418080017	10.529	52.71875	1.4181	81.25	2.5	0.016667	0.175485	0.878645833	
85	1.48353	1.461713249	10.286	51.71	1.4617	83.75	2.5	0.016667	0.171437	0.861833333	
87.5	1.527163	1.50534648	10.066	50.8025	1.5053	86.25	2.5	0.016667	0.167764	0.846708333	
90	1.570796	1.548979711	9.8717	50.015	1.549	88.75	2.5	0.016667	0.164528	0.833583333	

Example calculation of average cooling channel wall roughness continued.

92.5	1.61443	1.592612942	9.7076	49.36625	1.5926	91.25	2.5	0.016667	0.161793	0.822770833
95	1.658063	1.636246174	9.5772	48.875	1.6362	93.75	2.5	0.016667	0.15962	0.814583333
97.5	1.701696	1.679879405	9.4843	48.56	1.6799	96.25	2.5	0.016667	0.158072	0.809333333
100	1.745329	1.723512636	9.4327	48.44	1.7235	98.75	2.5	0.016667	0.157212	0.807333333
102.5	1.788962	1.767145868	9.4261	48.53375	1.7671	101.25	2.5	0.016667	0.157101	0.808895833
105	1.832596	1.810779099	9.4682	48.86	1.8108	103.75	2.5	0.016667	0.157803	0.814333333
107.5	1.876229	1.85441233	9.5628	49.4375	1.8544	106.25	2.5	0.016667	0.15938	0.823958333
110	1.919862	1.898045562	9.7137	50.285	1.898	108.75	2.5	0.016667	0.161895	0.838083333
112.5	1.963495	1.941678793	9.9246	51.42125	1.9417	111.25	2.5	0.016667	0.16541	0.857020833
115	2.007129	1.985312024	10.199	52.865	1.9853	113.75	2.5	0.016667	0.169987	0.881083333
117.5	2.050762	2.028945255	10.541	54.635	2.0289	116.25	2.5	0.016667	0.175689	0.910583333
120	2.094395	2.072578487	10.955	56.75	2.0726	118.75	2.5	0.016667	0.182578	0.945833333
122.5	2.138028	2.116211718	11.443	59.22875	2.1162	121.25	2.5	0.016667	0.190718	0.987145833
125	2.181662	2.159844949	12.01	62.09	2.1598	123.75	2.5	0.016667	0.20017	1.034833333
127.5	2.225295	2.203478181	12.66	65.3525	2.2035	126.25	2.5	0.016667	0.210997	1.089208333
130	2.268928	2.247111412	13.396	69.035	2.2471	128.75	2.5	0.016667	0.223262	1.150583333
132.5	2.312561	2.290744643	14.222	73.15625	2.2907	131.25	2.5	0.016667	0.237026	1.219270833
135	2.356194	2.334377875	15.141	77.735	2.3344	133.75	2.5	0.016667	0.252353	1.295583333
137.5	2.399828	2.378011106	16.158	82.79	2.378	136.25	2.5	0.016667	0.269305	1.379833333
140	2.443461	2.421644337	17.277	88.34	2.4216	138.75	2.5	0.016667	0.287945	1.472333333
142.5	2.487094	2.465277568	18.5	94.40375	2.4653	141.25	2.5	0.016667	0.308335	1.573395833
145	2.530727	2.5089108	19.832	101	2.5089	143.75	2.5	0.016667	0.330537	1.683333333
147.5	2.574361	2.552544031	21.277	108.1475	2.5525	146.25	2.5	0.016667	0.354614	1.802458333
150	2.617994	2.596177262	22.838	115.865	2.5962	148.75	1.25	0.008333	0.190314	0.965541667
152.5	2.661627	2.639810494	24.519	124.17125	2.6398	151.25				

Case	0	1	2	3	4	5	6	7	8	9	Unit
Height	6	7	8	9	10	12	14	16	18	20	mm
Width	6	5.143	4.5	4	3.6	3	2.571	2.25	2	1.8	mm
Ramanujan Perimeter	18.8	19.2	20.0	21.2	22.6	25.7	29.2	32.9	36.7	40.5	mm
Cross sectional area	28.274										mm ²
Channel length	203.2										mm
Channel wall surface area	3830	3899	4068	4304	4585	5229	5940	6687	7455	8237	mm ²
Channel volume	5745.345										mm ³

Case	0	1	2	3	4	5	6	7	8	9	Unit
Height	6	7	8	9	10	12	14	16	18	20	mm
Width	6	5.143	4.5	4	3.6	3	2.571	2.25	2	1.8	mm
Ramanujan Perimeter	18.8	19.2	20.0	21.2	22.6	25.7	29.2	32.9	36.7	40.5	mm
Cross sectional area	28.274										mm ²
Channel length	203.2										mm
Channel wall surface area	3830	3899	4068	4304	4585	5229	5940	6687	7455	8237	mm ²

Appendix C – Arduino code for thermocouple measurements.

```
/*
Colin Jack

This code is modified from the sample code found in the MAX31855 library.
It reads the multiplex data for all thermocouples and allows data to be copied to excel for analysis.
*/
#include <MAX31855.h>

#define FAULT_OPEN      10000 // No thermocouple
#define FAULT_SHORT_GND 10001 // Thermocouple short to ground
#define FAULT_SHORT_VCC 10002 // Thermocouple short to VCC
#define NO_MAX31855     10003 // MAX31855 not communicating

// Pin connections to the MAX31855x8 board
// The power requirement for the board is less than 2mA. Most microcontrollers can source or sink
a lot more
// than that one each I/O pin. For example, the ATmega328 supports up to 20mA. For
convenience, the board
// is placed directly on top of a row of I/O pins on the microcontroller. Power is supplied to the
board by
// holding the GND pin low and the VIN pin high
#define GND 3
#define T0 4
#define T1 5
#define T2 6
#define VIN 7
#define MISO 8
#define CS 9
#define SCK 10

// Create the temperature object, defining the pins used for communication
MAX31855 temp = MAX31855(MISO, CS, SCK);

void setup() {
  // Display temperatures using the serial port
  Serial.begin(9600);

  // Initialize pins
  pinMode(GND, OUTPUT);
  pinMode(T0, OUTPUT);
  pinMode(T1, OUTPUT);
  pinMode(T2, OUTPUT);
  pinMode(VIN, OUTPUT);

  // Power up the board
```

```

digitalWrite(GND, LOW);
digitalWrite(VIN, HIGH);
delay(200);
}

void loop () {
  // Display the junction temperature
  float temperature = temp.readJunction(CELSIUS);
  Serial.print("J=");
  printTemperature(temperature);

  // Display the temperatures of the 8 thermocouples
  for (int therm=0; therm<8; therm++) {
    // Selects the thermocouple based on 3-bit binary selector (000-111)
    digitalWrite(T0, therm & 1? HIGH: LOW);
    digitalWrite(T1, therm & 2? HIGH: LOW);
    digitalWrite(T2, therm & 4? HIGH: LOW);
    // The MAX31855 takes 100ms to sample the thermocouple.
    // Wait a bit longer to be safe. We'll wait 0.125 seconds
    delay(125);

    temperature = temp.readThermocouple(CELSIUS);
    if (temperature == FAULT_OPEN)
      continue;
    Serial.print("\tT");
    Serial.print(therm);
    Serial.print("= \t");
    printTemperature(temperature);
  }
  //verifyMAX31856();
  Serial.println();
  //delay(1000);
}

// Print the temperature, or the type of fault
void printTemperature(double temperature) {
  switch ((int) temperature) {
    case FAULT_OPEN:
      Serial.print("FAULT_OPEN");
      break;
    case FAULT_SHORT_GND:
      Serial.print("FAULT_SHORT_GND");
      break;
    case FAULT_SHORT_VCC:

```



```
    Serial.print("FAULT_SHORT_VCC");  
    break;  
case NO_MAX31855:  
    Serial.print("NO_MAX31855");  
    break;  
  
default:  
    Serial.print(temperature);  
    break;  
}  
Serial.print(" ");  
}
```

Appendix D: Experimental Data Example and Calibrations

Temperature Data Correction				
Block	Inlet_A	Inlet_B	Outlet_C	Outlet_D
B1	0.182	0.026	-0.103	-0.104
B2	0.074	0.034	0.055	-0.164
B3	-0.025	0.005	0.082	-0.062
B4	0.084	0.117	-0.055	-0.146

Data summary from one experimental run of block B2.

Same flow rate as #18								Initial flow	Final flow
Rate of heat transfer							100	157	157
Combined interpolated avg	1041.72	W					10	2	7
Inner interpolated avg	1059.058	W					1	0	6
Outer interpolated avg	1024.382	W	-34.676				0.1	6	7
Inner raw avg	1027.814	W					0.01	8	3
Outer raw avg	1375.7	W							
Combined raw avg	1201.757	W							
Heat Block Avg Temp	0.000	C	=		32	F			
Coolant temperature increase	0.704								
T_room		C							
Griddle Temperature	300	C							
Experimental time	10	min	=		600	seconds			
Initial total flow	15720.68	gal							
Final total flow	15776.73	gal							
Experimental flow	56.05	gal							
Flow rate	5.605	gal/min	=		0.353621	kg/s			
					Inlet_A	Inlet_B	Outlet_C	Outlet_D	
Corrective factors					0.074	0.034	0.055	-0.164	
Raw Average					17.560	17.818	18.512	18.490	C
Local raw avg					17.689		18.501		C
Corrected Average					17.634	17.852	18.568	18.326	C
Local Corrected avg					17.743		18.447		C
Stdev					0.183	0.147	0.158	0.142	C
Min					15.000	16.750	16.000	16.250	C
Max					18.250	18.500	19.250	19.000	C